# A robust material for the production of microfluidic liquid-liquid extraction chips

Rémy de Jong

Delft University of Technology

TU Delft

# Evaluation of a robust ALD coating to reduce irradiation-induced surface modifications on polymers and quartz for the usage of microfluidic liquid-liquid extraction chips

by

Rémy de Jong

In fulfillment of the requirements for the degree of
Master of Science

At the Delft University of Technology,
to be defended publicly on Friday, February 25, 2022.

| | |
|---|---|
| Daily supervisor: | A. Santoso |
| Thesis committee: | Prof.Dr.Ir. J.R. van Ommen |
| | Dr.Ir. R.M. de Kruijff |
| | Prof.Dr. S.J. Picken |
| Institution: | Delft University of Technology |
| Place: | Faculty of 3mE, Delft |
| Project Duration: | April, 2021 - February, 2022 |

TU Delft

# Preface

This thesis has been quite a journey with many ups and many downs. It has been a real challenge, and I would like to thank everybody for their support. However, there are a few people I would like to mention specifically. First of all, my daily supervisor Albert Santoso for the guidance he gave me during my project. He was always available to discuss this topic or when equipment I used needed to be fixed and for a casual chat. I want to thank Robin de Kruijff and Ruud van Ommen for their advice on the monthly meetings and available time for my questions. Furthermore, I would like to thank Stephen Picken for being part of my committee.

*Rémy de Jong*
*Delft, February 2022*

# Abstract

Microfluidic extraction is a promising alternative for existing extraction methods of radioisotopes due to the high surface-to-volume ratio. When assessing the compatibility of microfluidic material with the extraction system, there are three critical aspects—compatibility with organic solvents, compatibility with the radiochemistry, and, most importantly, the resistance to radiation-induced damage. Resistance to radiation-induced damage includes the primary reactions of the radiation with the matter, such as bond cleavage and the indirect damage caused by radiation due to free radicals. On the other hand, polymers are an interesting alternative as they are cheap and suitable for producing microfluidic chips. Therefore, in this experimental study, multiple interactions with polymers and quartz caused by radiation are assessed.

In general, most radiation-induced modifications can be traced back to changes taking place in the structure of the material. Some of the changes have been attributed to the scission of the polymer chains, promotion of cross-linkages, breaking of covalent bonds, formation of carbon clusters, and liberation of volatile products. However, these materials must not lose their mechanical and chemical properties to maintain a well-functioning microfluidic extraction system. Atomic layer deposition (ALD) is an interesting surface modification method due to its self-limiting nature and atomic precision control. With ALD, it is possible to deposit a nano-scale layer of metal oxide that reduces surface-induced damage without changing much of its bulk properties. Furthermore, with ALD, it is possible to change the wettability of the material to make them suited for microfluidic liquid-liquid extraction.

This study showed that a 40nm $TiO_2$ thin-film was able to stabilize the surface modifications during high flux electron irradiation. A similar pattern is found between the samples coated with VALD as radiation-induced surface activation is achieved. Briding oxygen that usually is present on the surface gets replaced by carboxyl groups and increases the surface energy to increase the hydrophilicity of the surface. Furthermore, polycarbonate, quartz, and high-density polyethylene showed impressive radiation resistance up to 5MGy as Young's modulus showed no significant difference. With this study, it is possible to use nano-coating to stabilize the radiation-induced surface activation and can be helpful for surface modifications in multiple fields.

# Contents

# Nomenclature

## Abbreviations

| Abbreviation | Definition |
|---|---|
| AALD | Atmospheric atomic layer deposition |
| ACA | Advancing contact angle |
| AFM | Atomic force microscopy |
| ALD | Atomic layer deposition |
| Bq | Becquerel |
| BSE | Backscattered electrons |
| CB | Cassie-Baxter |
| FTIR | Fourier-transform infrared spectroscopy |
| HDPE | High-density polyethylene |
| ICP-OES | Inductively coupled plasma - optical emission spectrometry |
| LLE | liquid-liquid extraction PC |
| Polycarbonate | |
| PDMS | Polydimethylsiloxaan |
| PE | Photon electric effect |
| PS | Polystyrene |
| RCA | Receding contact angle |
| Risa | Radiation induced surface activation |
| SE | Secondary electrons |
| VALD | Vacuum atomic layer deposition |

## Symbols

| Symbol | Definition | Unit |
|---|---|---|
| | | |
| $\alpha$ | Alpha particle | |
| $\beta$ | Beta particle | |
| Bq | Becquerel | $s^{-1}$ |
| $\gamma$ | gamma | |
| $\Theta$ | Angle | [Degrees] |

# List of Figures

# List of Tables

# 1 Introduction

Globally, cancer is the second leading cause of death. In 2018, it was estimated that cancer accounted for 9.6 million deaths worldwide, and that number continues to grow[1]. Therefore it is crucial to detect and treat this disease in an early stage to increase the survival rate. Among many techniques, medical radioisotopes stand out due to their diagnostic and therapeutic purposes, such as Ga-68, Ac-255, Tc-99m, and many others. For example, Ga-68 is a positron emitter used to diagnose cancerous tumors. Currently, reactors and cyclotrons are used for the production of the majority of medical isotopes. For both methods, the shorter half-life daughter nuclide needs to be separated from the longer half-life mother nuclide. When it comes to separation, there are multiple important aspects, including purity, efficiency, and time. Therefore, the separation is critical and often done via column chromatography. However, the separation with column chromatography requires pure mother isotopes due to the limited adsorption capacity of these columns [2].

An interesting alternative for column chromatography is microfluidic liquid-liquid extraction. During this separation method, two immiscible liquids flow next to each other; an extracting phase and an origin phase, from which the dissolved radioisotope needs to be extracted. Microfluidic extraction becomes lucrative due to the high surface-to-volume ratio. This results in an increased mass transfer and extraction efficiency compared with a batch with non-ideal mixing within a certain time period. By varying the flow rate and geometry, a more controlled environment is provided for the reaction, which results in a higher radiochemical yield and a higher molar activity, indicating a higher radiochemical purity[3, 4, 5, 6].

What microfluidic liquid-liquid extraction makes interesting is that two liquids can flow past each other in a microfluidic chip. This is possible because the surface tension and friction forces dominate over gravity. Therefore, surface tension is one of the most important factors to look into. The wettability and, subsequently, the contact angles are the best way to characterize the surface energy [5]. By adapting the surface tension in the channel, it is possible to create a phenomenon called interface pinning, where half of the channel attracts one phase but repels the other and, vice versa [7]. So for interface pinning to occur, the wettability of the two liquids with the surface of the chip needs to have a sufficiently large difference. To change the wettability of the material it is needed to modify the surface. One way to modify the surface is with atomic layer deposition (ALD).

However, there are some essential aspects of the microfluidic chip used for the extraction. For example, the design, compatibility of the material, the extraction fluids, and the operating conditions[8, 2, 9]. Numerous studies looked into the design, the extraction fluids, and the operating conditions [8, 9]. However, there is little research about the compatibility of the microfluidics chip material with the system. Most microfluidic chips for liquid-liquid extraction have been made out of silicon and glass because of their compatibility with organic solvents [5].

When it comes to assessing the compatibility of microfluidic material with the extraction system, there are three important aspects—compatibility with organic solvents, compatibility with the radiochemistry, and the resistance to radiation-induced damage. Compatibility with organic solvents has another two aspects. Firstly, the solubility of a solvent in material influences the swelling of the material. Secondly, the dissolution of the material is insolvent since these particles can be potential contaminants in the product. Resistance to radiation-induced damage includes the primary reactions of the radia-

tion with the matter, such as bond cleavage. For the indirect damage caused by radiation due to free radicals, it is important that the material is compatible with radiochemistry.

The goal of this paper is to find potential materials that have the most negligible effect on the induced gamma and electron radiation and can be used for the production of microfluidic chips. To provide a general comparison between different kinds of polymeric materials, a decision has been made to divide them into five groups: An aliphatic compound, a polymer with a carbon backbone and aromatic groups as functional groups, a polymer with aromatic groups inside the backbone, silicon-containing methyl groups, and a pure silicon dioxide. To determine which group would be the most suited for the production of microfluidic chips, multiple objectives need to be addressed.

The first objective is to characterize the changes of the surface properties and, in particular, the wettability. As stated above, the difference in wettability of the material is a crucial principle for the microfluidic system to work. The expectation is that the surface can be altered due to mechanical or chemical modifications induced by gamma/beta irradiation. Therefore, different characterization methods are needed to provide a clear image of the expected modifications.

The second objective is to check whether a thin-film coating can be used to influence this surface modification induced by gamma/beta irradiation. The thin film deposition by the ALD might not serve as a protective layer to decrease the damage induced by the radiation but might play an important role in the indirect damage caused by radiation due to free radicals.

That the thin film deposition might not serve as a protective layer brings us towards the final objective. How does the radiation influence the bulk properties of the material, and does the thin film deposition play a crucial role in reducing the radiation-induced damage will also be addressed in this paper.

# 2

# Theory

In this section, some background information on ionizing radiation is given. The general principle is explained, and different types of radiation are also elaborated. Thereafter, the effects of radiation on the mechanical properties and performance of polymers and quartz are explained. This is due to the fact that these materials are often used for the production of microfluidic chips. Finally, a brief explanation about surface energy and the water contact angle is given.

## 2.1. Radiation

Radiation is the emission and transmission of energy in the form of particles or waves through a medium. Radiation is often divided into two main categories: ionizing and non-ionizing radiation. For this experimental study, only ionizing radiation is relevant and will be discussed in more detail.

Ionizing radiation is a type of radiation that has sufficient energy to ionize the atoms. This means that the energy is sufficient enough that it can knock electrons out of the electron shell of an atom. Ionizing radiation can be released by atoms when they are unstable, in the form of electromagnetic waves (gamma or X-rays) or particles(neutrons, beta, and alpha). These unstable atoms are called radionuclides. The activity of a radionuclide is expressed in becquerel (Bq), and one becquerel is one disintegration per second. After a certain amount of time, which is dependent on the kind of radionuclide, half of the number of atoms is disintegrated. The time this process takes is called the half-life time of the radionuclide. The amount of damage ionizing radiation can induce is dependent on the type of radiation and how much of the dose is absorbed and is expressed in gray(Gy). A gray is the amount of joule absorbed by a kilogram of material. The effect of ionizing radiation depends on four factors: the type of radiation, the energy of the individual particles or photons, the number of particles or photons that strike the given area per unit of time, and the chemical nature of the material exposed to the radiation.

### 2.1.1. Different types of radiation

Based on the information provided in section 2.1 there are different types of radiation. Each with its characteristics and theoretically expected effects. In this section, the different types of ionizing radiation are discussed in more detail.

#### Alpha radiation

Alpha radiation consists of alpha particles that are created by isotopes of heavy elements with a Z-number higher than 83. As they tend to stabilize, by lowering their mass, they release two protons and two neutrons to form a helium-4 nucleus. This helium-4 atom is expelled, which is also known as $\alpha$ radiation. $\alpha$ radiation can be represented by the following:

$$ {}^{A}_{Z}X \longrightarrow {}^{A-4}_{Z-2}x' + {}^{4}_{2}\alpha \tag{2.1} $$

This decay mode by disintegration has a new element, with atomic Z number lowered by two, as a result. $\alpha$ particles are not very often used due to the extended risks of these emitters. $\alpha$ emitters can disperse spontaneously, which can result in an additional risk of internal contamination. $\alpha$ emitters are also more radiotoxic than $\gamma$ and $\beta$ emitters. Due to their double positive charge, alpha particles have a

tremendous ionizing effect. However, their mass is respectively high, which means that their main free path is low and thus result in very little penetration. For example, alpha particles of 4-10 MeV have a range of 5 to 11 cm in air and only a 20 to 100 $\mu$m in water [10].

**Beta radiation**
Beta-decay can occur when there are too many protons or neutrons in the nucleus. Beta-decay can be divided into two primary forms: beta-plus decay ($\beta^+$) and beta-minus decay ($\beta^-$). During $\beta^+$ decay, positrons and neutrinos are released, which results in a new nucleus where the atomic number (Z) is increased or decreased by one while the mass number (A) remains the same[11].

If a nuclide has a surplus of neutrons, it is unstable and radioactive. In order to achieve a more stable phase, one neutron within the nucleus is transformed into a proton. To cope with the conservation of energy, a negatively charged electron must be generated. This results in beta radiation. $\beta^-$ decay can be represented by the following relation 2.2.

$$\text{Negative beta decay } : {}^{A}_{Z}M \rightarrow {}^{A}_{Z+1}M + \beta^- + \bar{\nu} \tag{2.2}$$

The same goes up for a nucleus with a surplus of protons. In order to reach a more stable phase, one proton within the nucleus is transformed into a neutron. But now, a positively charged electron, also known as a positron, must be generated. $\beta^+$ decay can be represented by the following relation 2.3.

$$\text{Positive beta decay } : {}^{A}_{Z}M \rightarrow {}^{A}_{Z-1}M + \beta^+ + \nu \tag{2.3}$$

Beta particles are emitted with a continuous range of energies up to the maximum, which is characteristic for each radionuclide. Therefor the range [cm] of $\beta$ radiation can be expressed by equation 2.4. Where $0.5E_{\beta,max}$ is given in [MeV], $\rho$ in $[g * cm^{-3}]$. To give an indication of the range $\beta$ particles travel around 4 meter in air for each MeV [10].

$$R_\beta = \frac{0.5E_{\beta,max}}{\rho} \tag{2.4}$$

$\beta$ particles have four possible types of interaction:

- Elastic collisions with electrons
- Inelastic collisions with electrons
- Emission of Bremsstrahlung
- Emission of Cerenkov radiation

In the case of $\beta^+$ radiation there is also a fifth interaction possible

- Annihilation at the end of its path

**Elastic interaction**
Elastic interaction occurs when a $\beta$ particle collides with an electron that is firmly bound in the atomic shell without ejecting this electron from its orbit. The most important feature of this collision is that during the collision, no energy is transferred. However, it causes the $\beta$ particle to follow a winding path.

**Inelastic interaction**
Inelastic interactions lead to the most prominent energy transfer from the $\beta$ particles to the interacted matter. This collision leads to ionization, and this means that the material gets a positive or negative charge due to the loss of gain of an electron. The density of ionization is significantly smaller than that of $\alpha$ particles (with the same kinetic energy). But this also means that the range is significantly larger.

**Emission of Bremsstrahlung**
It is also possible that the $\beta$ particle comes close to the nucleus. If this happens, its trajectory is deflected due to the charge of the nucleus. In contrast to elastic interaction, there is an energy loss, which is released as electromagnetic radiation. The amount of energy (g) released is dependent on the Z-number of the nucleus and the energy of the $\beta$ particle($\beta$ max) (see equation 2.5).

$$g = 2 * 10^{-4} * Z * E_{\beta,max} \tag{2.5}$$

This interaction becomes more dominant for high energetic $\beta$ particles in combination with a high Z number. Therefore a nucleus with a low Z number is best suitable for shielding of $\beta$ radiation.

**Emission of Cerenkov radiation**
When the kinetic energy of the particle increases, the velocity also increases. When a $\beta$ particle has an energy of 250keV, it approaches the speed of light in a vacuum. However, the speed of light in a medium is dependent on the refractive index. So when a $\beta$ particle with high energy is emitted from the nucleus, its velocity may be higher than the velocity of light in the medium. If this is the case, the particle emits photons with a wavelength in the blue and violet region. This light is also known as Cerenkov radiation and is present in nuclear reactors.

**Annihilation**
Annihilation only happens when a $\beta_+$ is involved. When this $\beta_+$ is on the end of its path, it unites with an electron. The $\beta_+$ particle and the electron are converted into two photons of each 0.511MeV. Because the momentum of the two newly generated photons must add up to zero, they will both move in the exact opposite direction.

**Gamma radiation**
Gamma radiation consists of photons, which means that they have no charge or mass. This makes them different from $\alpha$ and $\beta$ particles. They diminish their velocity and lose their energy due to interactions with the material. For $\gamma$ photons, it is possible to not interact at all or to have an interaction where it loses all of its energy in one interaction. It can also transform into a new photon with lower energy. The type of interaction is dependent on the atomic number (Z) of the target, and the photon electron energy (E) as illustrated in Figure 2.1[12, 13].

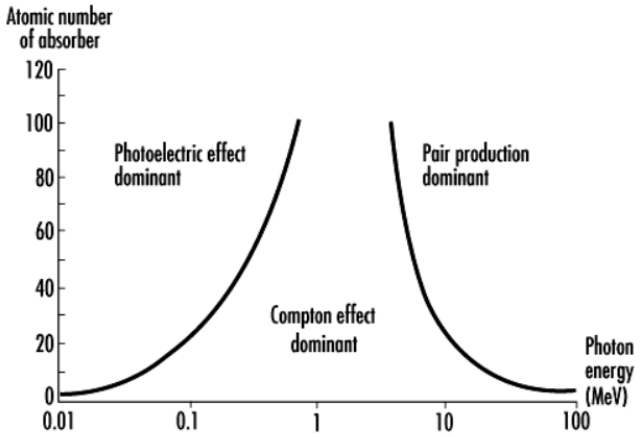


**Figure 2.1:** Relationship between mode of energy deposition, energy of incident photon, and Z number of absorber[14]

The photoelectric effect occurs, depending on the Z number, from 0-1 MeV. The incident photon disappears, and its energy is transferred to an electron of the target atom. When the energy is absorbed, the electron is ejected out of its orbit and acquires kinetic energy that of the energy of the photon minus the binding energy of the electron in that specific orbit. The hole created in the shell resulting from this interaction is directly filled by an electron from one of the outer shells, which generates X-ray photons. The probability of this effect is dependent on the Z number of the nucleus and is proportional to $Z^4$.

Due to this property, X-ray photons can give us much information about the difference in the Z number between materials. The photoelectric effect is most important at low energy levels, as illustrated in Figure 2.1.

Compton interaction occurs mainly with electrons that are not strongly bound. The original incoming photon disappears, and a photon with lower energy is created. This lower energy photon is referred to as the Compton photon. The electron is ejected with the remaining energy as kinetic energy. The amount of energy is transferred over the electron and photon depends on the angle the Compton photon is ejected. At a total reflection (180 $^{\circ}$), the energy of the electron is at its maximum. However, if the photon only touches the electron slightly and does not collide, then no energy is transferred.

Pair production is the opposite of the annihilation discussed above. When a photon transforms into a positron, an electron pair production occurs. This can only happen when the energy of the incoming photon is higher than the annihilation energy (1,022keV). The difference between the two energies is taken up by both particles in kinetic energy. Pair production becomes more relevant when the energy of the photon and the z number of the material increases because this process only occurs when there is a strong electric field.

### 2.1.2. Effect of radiation on the mechanical properties and performance of polymers

While the previous subsection discussed the different effects of radiation due to its source, this subsection will focus on the different effects of radiation due to the type of the exposed substrate. Essential aspects to take more into detail change in the morphology, structure, surface, and chemical bonds of the material. For this literature, the main focus lies on polymeric material and glass.

The number of radioactivity processed in a microfluidic chip can lead to radiation-induced material decomposition, such as breaking of the main chains, changes in the number of double bonds, and the emission of volatile products. This can lead to impurities that can contaminate the product and affect the process. Furthermore, the damage induced by radiation can also lead to fatigue of hardware components [6]. The interaction between the radiation and the material can be characterized by linear energy transfer (LET). This is the amount of energy that is deposited by an ionizing particle in the material per unit of distance. Low-LET interactions are caused by electrons or gamma rays. A high-LET will attenuate the particle more quickly and are caused by alpha particles. However, a high-LET often means that the particle has a greater interaction volume with the material. When the material is irradiated, large amounts of energy are transferred, which can lead to radical production. The degree of degradation is dependent on the different types of degradation. These depend on different factors, such as the presence of light, oxygen, and other agents.

The early classification was that some polymers undergo chain scissions, which is a random rupture of the bond that reduces the molecular weight of the polymer. Where other polymers undergo cross-linking or chain branching, which has as a result that the polymer forms a large molecular network[15, 16, 17]. Branching creates a more amorphous structure with linear polymer chains, and cross-linking contains a matrix of branches. However, this classification is not as simple as it seems due to the high sensitivity of polymers to their environment, especially when oxygen is present[18, 19]. In general, most of the polymers have an average resistance to radiation and can tolerate moderate doses of 1-10 kGy without little to no degradation in the mechanical performance and properties[20]. However, to protect the backbone of the polymer against high radiation doses up to 1 MGy, it needs efficient additives to prevent the chain reaction of oxidative degradation[18]. This additive acts as a stabilizer that can take in excessive energy without changing the molecular structure.

The majority of the studies performed on radiation stability concerning polymeric systems have been focused on either $\gamma$ photons or electrons. The mechanism that is the most important for energy loss is Compton scattering, where the photon interacts with an electron in the shell and causes an ejection of the electron. The probability is dependent on the electron density of the material [21]. Polymers consist of long molecular chains which can be broken due to the absorption of energy above the binding energy of the covalent bond of the main chain. The energy of these bindings are in the range of 5 - 10 eV and are easily surpassed by the energy of beta and gamma radiation which has an energy in the range of 1 to 10 MeV. This can lead directly to the formation of radicals which cause a high risk of degradation

to all kinds of polymers[22].

**Crosslinking and chain scission**
The primary radiation interaction is caused by the initial interaction of gamma-ray photons with the electrons of the polymers. The photons cause ejections of secondary electrons, which brings the polymer to an excited state. Most of the time, a breakage occurs at C-H bonds despite the lower bond energy that a C-C bond has. This can be attributed to the energy distribution along the backbone, which is not possible in C-H bonds. The free radicals produced during this bond breaking and the addition of unsaturated sites lead to chain branching and/or cross-linking, as seen in Figure 2.2. In this figure, multiple interactions are illustrated, such as the formation of hydrogen radicals, irreversible hydrogen loss, double bond formation, and cross-linking.

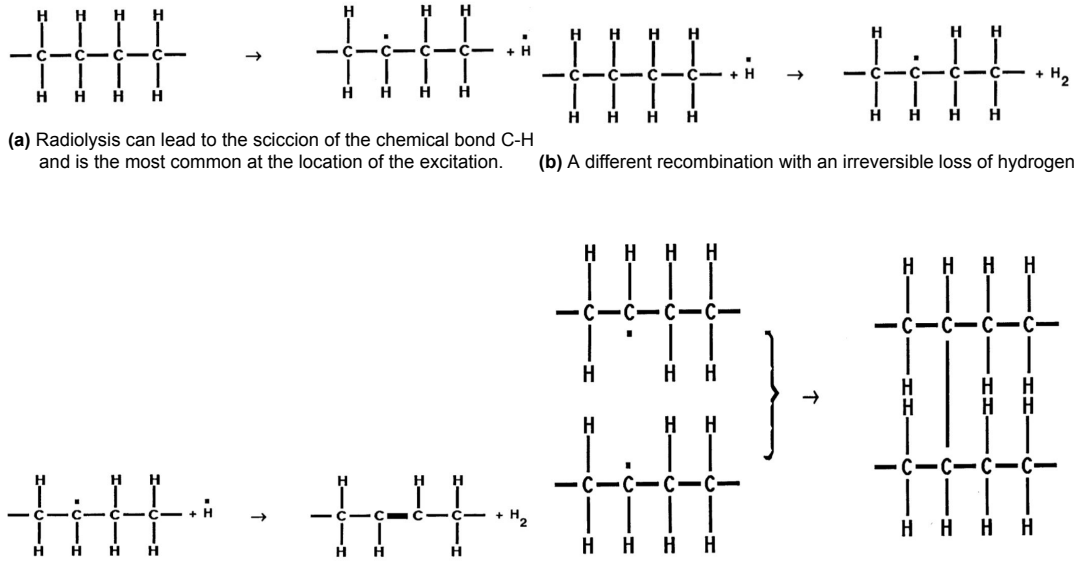

**(a)** Radiolysis can lead to the sciccion of the chemical bond C-H and is the most common at the location of the excitation.

**(b)** A different recombination with an irreversible loss of hydrogen

**(c)** When two events happen on the same chain a double bond formation can occur

**(d)** When two double bonded chains recombine it results in cross linking of the polymer chains.

**Figure 2.2:** Main radiolysis effects on polymers[23]

According to Wypych et al. and Chapiro et al.[22, 17], chain scission is more likely to occur on a surface where oxygen is available because oxygen induces the degradation processes even for polymers that prefer to cross-link. However, cross-linking has a higher probability at the core of the sample, where the energy of the radiation is transferred, but oxygen is not available.

In general, polymers that possess aromatic groups have superior radiation stability than the aliphatic polymers discussed above. These aromatic groups can be located in the backbone of the polymer or added as additives[24, 20]. The aromatic rings can dissipate a large amount of the excess energy from the gamma-ray photons. However, when exposed to high-energy ion irradiation, the aromatic ring will lose its aromatic conjugation. This results in less dissipation of the excess energy from the gamma-ray photons[25].

While cross-linking and branching increases the average molecular weight. Chain scission decreases the average molecular weight of the polymer. Both can occur at the same time, and the degree of these reactions is proportional to the radiation dose. However, it does only depends a little on the type of radiation [21, 26]. To quantify the radiochemical yield, the G value is used. This value refers to the number of products formed or the number of molecules of reactant consumed per 100eV of energy absorbed.

**Mechanical properties**
The reactions that take place during irradiation can change the molecular structure of the material. In particular, chain branching, scission, and cross-linking. As stated in the previous section, chain branching and cross-linking increase the molecular weight of the polymer while degradation and chain scission

decrease the initial molecular weight of the polymer. These molecular modifications can change the mechanical properties of the material.

To test how the ionizing radiation changes the properties of the material, the tensile test is the most sensitive to modification induced by radiation. This is due to the fact that the molecular weight and crystallinity are two crucial factors that determine the mechanical behaviour[27].

The increase in crystallinity and the molecular weight of the chains due to cross-linking causes an increase in the Youngs elastic modulus. However, the cross-linking reduces the free movement of the molecular strings, and this goes paired with the elongation at break, which is related to the brittleness of the material. Thus a high elastic modulus is related to a high-stress level and tends to increase the strength but reduces the elongation at break. When chain scission occurs, it generally deteriorates the material's mechanical properties. It strongly reduces the elongation at break and decreases the general strength of the material[27, 28].

**Radiation-induced oxidation**
In the previous section, it was already mentioned that the irradiated polymers react differently in the presence of oxygen. The quantitative and qualitative degradation of the processes is affected. It can increase the rate of degradation and the type of cross-linking and chain scission [29]. In general, when aromatic and aliphatic polymers are oxidized, it leads to the emergence of stable by-products such as alcohols, ketones, and carboxylic acids. During the reaction, free radicals (R·) react with molecular oxygen and hydroperoxides and prevent them from attacking the polymer chain. This reaction prevents the polymer from cross-linking. However, such polymers are more prone to scission [30]. This can initiate new chain reactions in predominately amorphous regions because, in an ordered crystalline structure, oxygen is unable to penetrate. Therefore, it's different for each polymer which reaction, cross-linking or chain scission, predominates in the presence of oxygen.

### 2.1.3. Radiation effects in ceramics and crystals

Ceramics and crystals are available in a wide variety, which means that they differ in composition, structure, and applications. However, the response of ceramics when irradiated shows substantial similarities and sufficient commonality that they can be described in ensemble[31].

The primary radiation damage is the displacement of one or more atoms or the formation of Frenkel defects. A Frenkel defect is a point defect in a crystalline solid. This defect is formed when an atom or an ion leaves its place in the lattice, creating a vacancy. Furthermore, these atoms or ions can occupy a site in the crystal that is normally unoccupied. Firstly, these kinds of displacements may occur by the transfer of the kinetic energy of the incident projectile (electron, proton, neutron, ion). Secondly, it may occur through the conversion of radiation-induced excitations in ion movements. The accumulation of these primary displacements can result in defect recombination, aggregation, and amorphization, which are elaborated below[32].

**Defect recombination**
Crystals and ceramics consist of one or more sub-lattice, which can de be distinguished by distinct atoms types. These atoms may have similar or different masses and radii than each other. The change in their masses also means that they have a different binding energy. So there is a difference in the probability that a defect is formed due to the excess energy from the incident particle. Furthermore, these lattice structures are, in general, not close-packed, and there are interstices sites available to which the dislodged ions can bind. These displacements may result in a change of charge.

**Defect aggregation**
The defects preferably want to undergo recombination. However, for the defects that do not undergo recombination, defect aggregation is needed to reduce the elastic energy. This means that a structure is formed from fragments or particles. Nevertheless, this can also lead to vacancy aggregation, which leads to void formation.

**Amorphization**
Defect aggregation is a localized secondary defect response to the primary displacements discussed above. A more likely response to deal with the individual defects is that the entire solid adopts a uniformly defective state, which is a worst-case scenario that leads to the loss of the long-range crystalline structure[32].

**Radiation induced surface activation of metal oxides**
When a metal oxide is irradiated by radiation, the surface becomes more hydrophilic and is also known as radiation-induced surface activation (RISA). According to Honjo et al., in ambient air, hydrophilicity increased as the duration of irradiation became longer[33]. While in the air with a dehumidification agent, the hydrophilicity enhancement rate tends to be lower. With XPS analyses, three peaks could be identified (a) oxygen in bulk, (b) surface bridging oxygen, and (c) adsorbed hydroxyl radicals. There was a slight decrease in the bridging oxygen surface density and an increase in the hydroxyl group. Therefore, it was found that the adsorbed hydroxyl group increased along with the hydrophilicity.

## 2.2. Contact angle

To get an idea of how rough a surface is, there is being looked at the wetting property. It is used to measure the disintegration and dissolution of a solid surface. The wetting property is usually described with the contact angle of a sessile droplet of water. The contact angle represents the hydrophobicity and hydrophilicity of a surface. It is important to consider two factors. The first factor is the relationship of the energy of the solid vapor interface ($\gamma_{SV}$), the surface energy of the liquid-vapor interface, and the solid-liquid interface. This can be expressed by the Youngs equation, which relates to the contact angle ($\Theta$) [34].

$$cos\Theta_c = (\gamma_{SV} - \gamma_{SL})/\gamma_{LV} \tag{2.6}$$

The second factor which needs to be considered is the geometry of the solid surface. The type and degree of roughness and porosity play an important role. This is also highly dependent on the handling, and the treatment of the sample [34].

The advancing angle($\Theta_A$) is made by placing the needle close to the surface and start injecting the liquid onto the surface. During the measurement, water is added, which means that the shape of the droplet is changing. When the baseline of the droplet contacting the surface remains stable, the ACA is reached.

During the receding contact angle (RCA) measurement, water is first removed from the initial drop. The volume of the droplet starts decreasing, and eventually, the length of the baseline will decrease. This represents the RCA. It is important to note that a droplet smaller than 3$\mu$l does not provide reliable data as the needle will distort the measurement[35].

The difference between the RCA and ACA is called the contact angle hysteresis as stated in equation 2.7 and provides insight on the surface roughness concerning the contact angle.

$$H = \Theta_A - \Theta_R \tag{2.7}$$

Theoretically, the hysteresis contact angle should be 0° if the sample has a homogeneous surface[36, 37]. However, in reality, a surface is, most of the time neither perfectly flat. Therefore, Wenzel proposed an equation (2.8) that considers the surface and roughness.

$$cos\theta^W = rcon\theta \tag{2.8}$$

In this equation, the apparent contact angle is represented by $\theta^W$, r is the roughness factor, and $\theta$ refers to Young's contact angle. Wenzel's theory is based on the assumption that the liquid follows the roughness of the surface to enter the grooves of the surface. So, according to Wenzel's equation, roughness can enhance, depending on its surface energy, the hydrophobicity, and hydrophilicity of the surface[38].

If the surface is extremely rough, it becomes hard for the water to enter the grooves because of the air that is trapped inside it. This means that the droplet rests on the pockets of air and only the top of the surface, as seen in Figure 2.5. If this happens, the droplet is in the Cassie-Baxter (CB) state and follows the Equation 2.9.

$$\cos\theta^{\mathrm{CB}} = f(1 + \cos\theta) - 1 \tag{2.9}$$

Where $\cos\theta^{CB}$ represents the apparent contact angle. f is the fraction of the surface that is in contact with the droplet and, $\theta$ represents Young's contact angle. According to the CB equation, we need a very small f to have a hydrophobic surface[38].

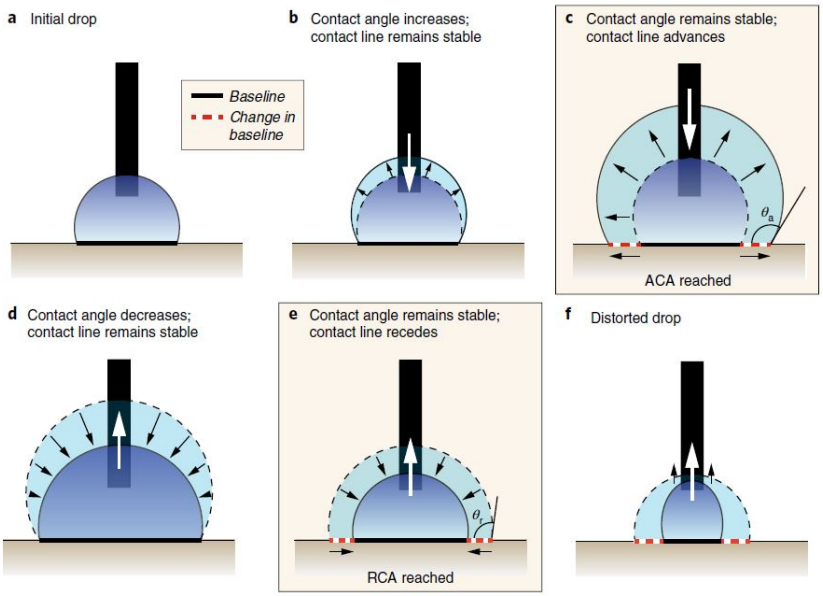


**Figure 2.3:** Different stages of the ACA and RCA measurements[35]

**(a)** The white arrow represents the direction of the water flow during the measurement and tells if water is pumped out or in the droplet. **a)**, A droplet of a 1-3 $\mu$l is placed. **b)**, water is pumped in, and the droplet is expanding, but the baseline remains stable. At this stage, the ACA is not reached yet. **c)**, When the baseline starts increasing, the ACA is reached, but water is still pumped in until a droplet of around 8 $\mu$l is formed. **d)**, For the RCA measurement, the water is first removed. The shape of the droplet changes, but the baseline remains stable. At this stage, the RCA is not reached yet. **e)**, When the baseline starts decreasing, the RCA is reached. **f)** when a droplet becomes smaller than 3 $\mu$l, it will be distorted by the needle, and it is not possible to receive reliable data[35].

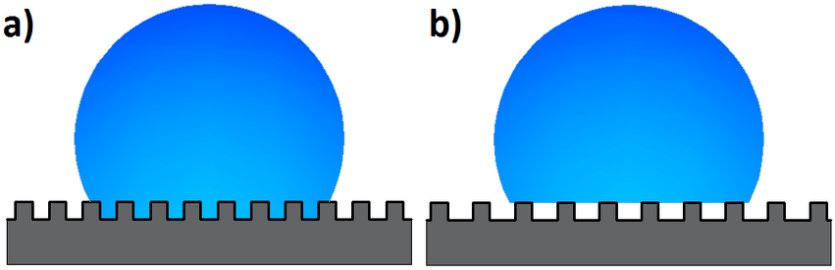


**Figure 2.5:** Representation of (a) Wenzel and (b) Cassie-Baxter models[39]

.

Measuring the RCA and ACA has several advantages. Firstly, is that the RCA and ACA tend to overcome many of the metastable free energy spots. This means that the local minima where a droplet may rest are overcome. Secondly, the measured hysteresis values give insight into the surface heterogeneity and how much water adheres to the surface. Finally, if only a static droplet is used during the measurement, evaporation may affect the contact angle. This is neglected during an ACA and RCA measurement[37].

## 2.3. Atomic layer deposition

Microfluidic chips used for liquid-liquid extraction must satisfy a broad range of requirements such as radiation stability, solvent compatibility, and need the right wettability. As discussed in section 1, for interface pinning to occur, the wettability of the two liquids with the surface of the chip needs to have a sufficiently large difference. To meet this requirement, surface modification is needed. In this section, Atomic layer deposition techniques are discussed that are suitable to achieve this interface pinning. As discussed in Section 2.1 the range of alpha, beta and gamma are sufficient to penetrate the coating of a few nanometers. So, this section won't focus on radiation protection. Note that it is interesting to look into the chemical composition of the coating when it contains oxygen.

Atomic layer deposition (ALD) is a technique that is based on vapor gas phase deposition. With

ALD, it is possible to deposit a layer of material with a thickness of a few nanometers on the substrate due to the self-limited surface reactions[40, 41]. This process involves the substrate's surface being exposed to alternating precursors with a purge step in between as illustrated in 2.6. First, the substrate is exposed to the first precursor during the first pulse for a designated amount of time. This allows the precursor to react with the surface of the substrate. Thereafter, the chamber is purged with an inert carrier gas that is able to remove any of the unreacted precursors and reaction by-products. After this purge, the second precursor is released in the chamber, which replaces the ligands of the first precursor. To make sure that any unreacted precursor or any by-product is removed, the chamber is again purged. This process is repeated for a certain number of cycles to create a nanolayer of a certain thickness on the substrate. The primary advantages of ALD are derived from the self-saturating gas-surface reaction control of the deposition process[41]. ALD has a uniform deposition and is often a critical reason to pick ALD above other techniques such as chemical vapor deposition[41, 42].

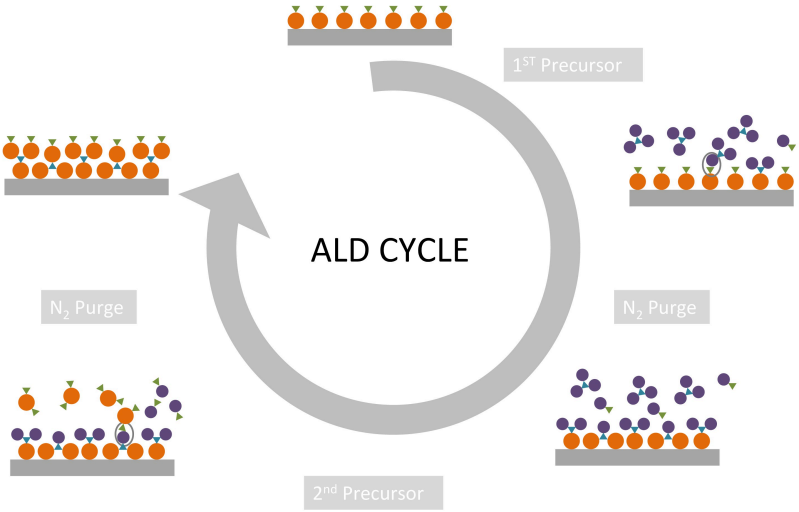


**Figure 2.6:** Schematic representation of an ALD cycle[40]

.

The temperature plays an important role in the ALD process and determines the growth saturation. When the temperature is too low, some reactants tend to condensate on the surface. When this is too high, the reactant can decompose. This range of temperature is referred to as the ALD temperature window. When the temperature is outside this window, it results in poor growth rates and non-ALD type depositions[41]. Thus, in order to utilize the ALD to its full potential, it is important to operate within the ALD temperature window.

Another advantage is that ALD processing can also be performed on large substrates and on multiple substrates simultaneously. The gas-phase molecules are diffused in the reactor chamber, where it fills up all the space independent of the substrate geometry. So, only the size of the reaction chamber is a limiting factor[42]. If the precursor pulse time is sufficient, it can disperse into deep trenches. This allows for a complete reaction to the entire surface. The whole surface will not react simultaneously due to different precursors gas fluxes[42].

Most ALD processes are performed in combination with a vacuum pump. This makes it possible to move the reactants around through the reactor without compromising the environment of the reactor. However, ALD can also be performed under atmospheric pressure. The reactant and products are now pushed through the reactor, and the diffusion rate can be controlled by the flow of the gas.

### 2.3.1. Plasma enhanced ALD

The principle of Plasma enhanced ALD (PL-ALD) is to use plasma during the process to produce highly reactive ozone radicals to promote the growth of the substrate and decrease the operating temperature

of the ALD. However, PE-ALD also has some limitations. The plasma can not only create radicals that promote the growth of the atomic layer, but it can also trigger undesired side reactions with the substrate [40].

### 2.3.2. ALD on polymers

During an ALD, the first few cycles are not the same as the other cycles. The deposition relies on the reactant reactions with the substrate instead of the deposited material. This is also known as the ALD nucleation phase, and it depends on the chemistry between the surface and the reactants. Therefore, the type and density of the functional groups are rather important for the nucleation of the polymers. When the polymers have abundant reactive sites (i.e., hydroxyl groups), it makes the reaction with the surface possible. However, these reactions sites may or may not be present, depending on the polymer. Furthermore, most of the polymers are permeable to small molecules, which allows the ALD precursor to diffuse from the surface into the bulk of the polymer. After a few cycles of ALD, the deposited material is thick enough to cover the porous surface and reduces the diffusion of the reactants into the bulk of the polymer. Only when the nanolayer reaches a certain thickness, the diffusion of reactants is completely blocked. This thickness is dependent on the amount and density of the functional groups and also determines whether there is a well-defined interface between the polymer and the nanolayer[43, 44, 45].

To modify the wetting property of the surface of the material, a thickness of around 10 atomic layers is needed. This is not directly linked to the number of cycles needed to reach a conformal nanolayer because the growth per cycle is dependent on the film nucleation and growth. The nucleation domain is expected during the first 20 cycles. However, this also depends on the surface of the material and the reactants used for the ALD[44, 45].

## 2.4. Material selection

To separate radionuclides at a micro-scale, very robust microfluidic chips have to be fabricated. These chips need to satisfy a broad range of requirements such as chemical stability, solvent compatibility, thermal and high-pressure resistance. The main focus for this research lies in radiation resistance. Therefore, four types of polymers are elaborated: a siloxane (PDMS), a polymer with an aromatic ring as a side group (polystyrene), a polymer with an aromatic ring in the backbone (polycarbonate), and a polymer with a carbon backbone (High-density polyethylene). Furthermore, pure silliciumoxide (quartz) is also being assessed.

### 2.4.1. Polydimethylsiloxane

Polydimethylsiloxane(PDMS) is a mineral organic polymer; this means that the structure contains carbon and silicon. PDMS is categorized in the siloxane family and is used in a wide variety of applications such as food additives, shampoos, and is used for the fabrication of microfluidic chips.

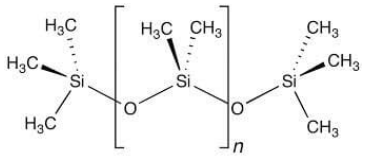


**Figure 2.7:** PDMS monomer[46]

The phase of PDMS is based on the size of the monomers chain and the number of non-crossed linked PDMS. The fragmented formula of PDMS is $CH_3[Si(CH_3)2O]nSi(CH_3)_3$, with n the number of monomers repetitions. A low n PDMS is more likely to be in a gel-like phase, while a high n PDMS seems to be solid. After crosslinking, PDMS becomes a hydrophobic elastomer with a WCA around the 100°[47]. There are a few significant advantages of PDMS. Firstly, it is easy to deform; this allows the integration of microfluidic valves and makes sure that the connections are leak-proof. Secondly, it is inexpensive compared with other materials. Thirdly, it is highly suitable for the production of microfluidic chips due to the fact that PDMS is pourable for a few hours after mixing with the cross-linking agent. At room temperature, the PDMS is cured within two days, but if the temperature is increased, it will only take a few hours [46].

PDMS provides a surface that has low free surface energy, good thermal stability, and is chemically inert. Furthermore, it is optically transparent. The physical properties of Sylgard 184-PDMS include a high tensile modulus(1.8MPa) and have a low thermal conductivity. PDMS is also impermeable to liquids but has a good permeability for gasses [48]. Surface modification for PDMS is often more challenging to control, which can be problematic when working with liquids. With a WCA around 100 °, PDMS is strongly hydrophobic, which can result in channels holding aqueous solutions to form air bubbles. However, PDMS can become distorted when they are in contact with organic solvents[6]. Furthermore, the surface molecules of PDMS are continuously replaced with the PDMS in the bulk[48]. This makes surface control of PDMS in the long term difficult.

When PDMS is exposed to ionizing radiation, it will undergo crosslinking with as main volatile products hydrogen, methane, and ethane gasses[21, 26]. Chemical changes in the molecular structure of PDMS were observed with the use of IR spectroscopy. Multiple Si-H and new -Si-O- structures were found. Studies with ESR revealed that under irradiation $CH_3\cdot$,$-CH_2\cdot$, $-Si\cdot$, and $-O\cdot$ were produced [21, 49]. According to Von white et al., radiation stability for PDMS seems to be quite high. They have been widely used in varying radiation environments, and minimal damage can be expected up to 1 MGy. However, at higher doses, the PDMS hardens, increasing the modulus. With a dose of 100kGy, the tensile elongation is nearly half of the original properties. [20]

### 2.4.2. Polystyrene

Polystyrene(PS) is a transparent non-polar thermoplastic that is widely used in semi-finished products like films, sheets, and foams. Due to the aromatic ring, it is not possible to form a crystalline structure that has excellent optical clarity as a result. It also has good chemical resistance to dilutes with a high and low PH. Due to the lack of a crystalline structure, PS has a low glass transition temperature (Tg) of about 100°. When PS is heated above this threshold, it can be easily molded. Because the backbone of the polymer only consists of carbon, it has a low impact strength and is brittle. However, it has a high to medium tensile strength(35-55Mpa). A significant limitation of PS is that it is attacked by hydrocarbon solvents and has poor oxygen resistance. There are no hydrophilic groups in the polymer which results in a high WCA of 87.4° [46].

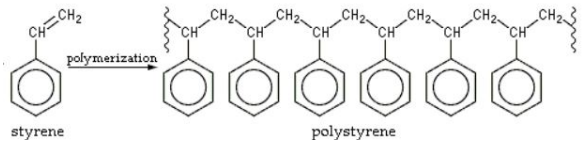


**Figure 2.8:** Polystyrene monomer [46]

PS undergoes mainly crosslinking under radiation; according to Charlesby et al., the yield of permanent chain scission is relatively small and can be neglected [26]. However, even when the crosslink reaction is dominating the radiation chemistry, the overall yield is still minimal if PS is compared with other nonaromatic polymers. This is the result of the presence of the benzene ring that can dissipate a large amount of excess energy. The primary volatile product is hydrogen and is only produced in small yields with a $G(H_2) = 0.022 - 0.026$ [30]. The backbone of PS contains two carbon atoms and are potential sides for oxidation. According to FT-IR studies performed by Vardhan et al., it seems that the alkyl radicals form C=O, and also O-H bonds formation is noticed [15]. However, research by O'Donnell et al. stated that when PS is placed in an oxygen-rich environment, the PS radicals, which generally contribute to crosslinking, react with the oxygen to form peroxides. These peroxides decompose, which leads to oxidative degradation of the main chain[50]. While the benzene ring is more stable against radiation, it is still possible that free radicals occur in the ring, which is suggested to be involved in the crosslinking reaction according to Hill et al.[21].

### 2.4.3. Polycarbonate

Polycarbonate(PC) is one of the most used thermoplastic, as it is amorphous and can be easily molded and thermoformed. PC is formed by the reaction phosgene and an aromatic dihydroxy compound, where the hydrogen chloride is eliminated. The most common diol used in the polymerization of PC is bisphenol A (BPA). PC has many exciting properties, such as a superb ability to transmit light, a high impact toughness, a high creep resistance, and good dimensional stability. The chemical resistance is

good against diluted acids, aliphatic hydrocarbons, and alcohols. Its Tg is about 151°[46]

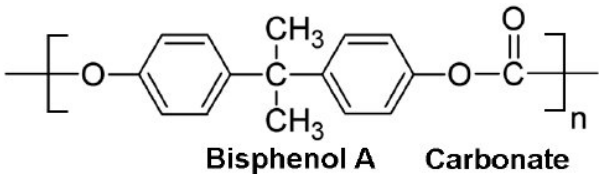


**Figure 2.9:** Polycarbonate [46]

The irradiation of PC has been studied for multiple years, especially the green coloration induced by radiation. This has been assigned to trapped electrons or a combination of trapped electrons and radical ions. PC undergoes mainly chain scission when placed in an environment where no oxygen is present. This is probably caused by the high sensitivity of the carbonate group to chain scission [21]. In a study performed by Golden et al., they examined the production of gases on irradiation. The major volatile products are carbon dioxide and oxygen, with small amounts of hydrogen, methane, and benzene [21]. A more recent study from Babanalbandi et al. showed nuclear magnetic resonance analysis peaks characteristic for phenol type chain end structures with G-value (0.7).

### 2.4.4. High density polyethylene

Polyethylene (PE) is categorized in the polyolefins class, which is the largest class of thermoplastics. PE can be processed by injection molding, blow molding, and thermoforming. The low cost, in combination with the easy process-ability and their good chemical and physical properties, makes them a prevalent choice. PE comes in many different grades, which differ in molecular weight, density, and branching. The degree of branching combined with the molecular weight of the polymer determines the mechanical properties and the Tg of the polymer. With a high polymer density comes a higher degree of crystalline structure, which results in a more rigid and stiffer polymer. HDPE has a good resistance against dilute acids, alkalis, and alcohol but poor resistance against hydrocarbons. High-density polyethylene (HDPE) has a low degree of branching, which results in a higher crystalline structure. This makes HDPE a dense and more rigid material that is less permeable than other types of PE. HPDE is often used due to its high strength and for applications where high chemical resistance is needed. It has a water contact angle of 95°[46].

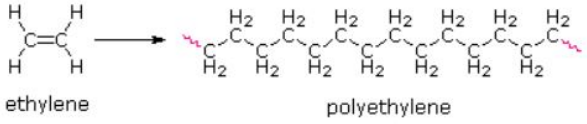


**Figure 2.10:** Polyethylene monomer[46]

When HDPE is irradiated, it undergoes mainly crosslinking effects [26, 21]. There is a bond breakage at the C-C connection. The alkyl radicals undergo radical, radical recombination with the other polymer strings. This can lead to H and Y crosslinking. The primary volatile product produced by irradiation of HDPE is hydrogen gasses, which are formed by the recombination of hydrogen atoms that are formed by the cleavage of C-H bonds. This recombination of hydrogen atoms is dependent on the grade of the crystalline structure of HDPE.

### 2.4.5. Quartz

Quartz is pure silicon dioxide and consists of a $SiO_4$ framework as seen in Figure 2.11. Quartz has a number of unique properties that make it a crucial material for the fabrication of high-tech products. A few of those properties are; high chemical, thermal, and radiation resistance, low thermal expansion, and high transparency. Quartz is excellent to withstand compressive strength. However, surface flaws can reduce the inherent strength drastically.

When quartz is irradiated with ionizing radiation, aggregation of molecular oxygen can occur. This means that from the Si-O bond and oxygen atom moves off-center to bond with another adjacent oxygen atom. These atoms can form an -O-O- peroxy linkage between Si atoms, creating an oxygen

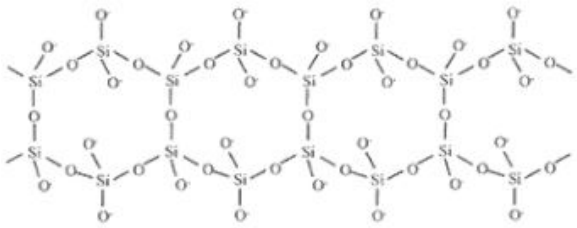

**Figure 2.11:** Continuous framework of $SiO_4$ silicon-oxygen tetrahedral

vacancy occupied with two electrons. These electrons originate from the Si orbitals. When one of these electrons leaves the vacancy, it causes the adjacent silicons to move into a triangular state instead of a tetrahedral state[32].

# 3

# Materials & Methods

This chapter explains the different materials, methods, and procedures used in this thesis. In the appendix C, additional information about some of the characterization methods are elaborated in more detail.

## 3.1. Materials

PDMS was the only polymer that was produced in the lab. The PDMS was fabricated by mixing polymer base and curing agent in a ratio of 10:1 (Sylgard 184 Elastomer Kit, Dow Corning Comp.) Next, the mixture was stirred manually for at least 2 minutes. To remove the air bubbles from the mixture, it was placed in a vacuum desiccator for 30 minutes. Once the vacuum desiccator removed all bubbles, the mixture was poured into a Petri dish and set back into a vacuum desiccator for at least 30 minutes. After that, the mixture was cured overnight in an oven at 70 $^{\circ}$C.

Polycarbonate (Poly bisphenol-A-carbonate) and high-density polyethylene were commercially found and bought from
$https://www.kunststofplatenshop.nl/$ and delivered as a plate with dimensions 200X200X4mm. The polystyrene originates from the Petri-dish (Sarstedt) available in the lab. Each sample used in this thesis was cut to slabs from around the same size of 5mm by 5mm except for quartz (Si-mat), pre-cut at 15mm by 5mm. After cutting, each slab was cleaned with adhesive tape to remove dust and other particles from the surface and cleansed with iso-propanol.

Some of the polymers were placed in a 1M $HNO_3$ solution during these experiments. This solution was made through dilution of $99$% pure $HNO_3$(Sigma Aldrich)

## 3.2. Atomic layer deposition

The $TiO_2$ deposition was carried out using two different ALD setups. The first setup is a home-built atmospheric-pressure ALD setup with a flat-substrate reactor. The second setup used is a Veeco Fiji G2 which operates at vacuum pressure. For the titanium precursor, Tetrakis(dimethylamino)titanium (TDMAT) was used, and ozone was produced using an ozone generator (Sander Certizon Ozoniser). The process parameters used during the ALD are shown in Table 3.1. For atmospheric ALD, longer pulse and purge times were utilized due to slower diffusion and convection limitations, such as dead zones in the reactor. In addition, during the atmospheric ALD, purging was done with an inert nitrogen gas flow, whereas in the vacuum ALD setup, the purging was done by pulling a vacuum.

## 3.3. Surface characterization methods

To identify the changes on the surface, several characterization methods are used. The water contact angle is a powerful tool to obtain information about the surface. However, techniques such as scanning electron microscopy and atomic force microscopy are used to gain more detailed information. To obtain more information about the chemical state of the surface, techniques such as X-Ray diffraction, X-Ray

**Table 3.1:** ALD parameters used for different ALD processes.

| ALD setup | Co-reactant used | Precursor pulse (s) | Precursor flowrate (l/min) | Co-reactant pulse (s) | Co-reactant flowrate (l/min) | Purge (s) | Purge flowrate (l/min) |
|---|---|---|---|---|---|---|---|
| Vacuum | O2 plasma | 0.06 | 0.06 | 0.25 | 0.06 | 45 | - |
| Atmospheric | O3 | 10 | 0.50 | 30 | 0.70 | 100 | 1.50 |

Photoelectron Spectroscopy, and Fourier-transform infrared spectroscopy are used. A more extensive explanation of the characterization methods can be found in Appendix C

### 3.3.1. Contact angle measurement

Advancing and receding contact angles( $\theta_A$ and $\theta_R$) were measured using a Krüss drop shaper analyzer. An automated dispensing system was used to increase and decrease the volume of a sessile droplet of demi-water on the surface. Meanwhile, the drop shape analysis software was used to measure the contact angles from the camera images. Each sample was measured at least four times on different positions on the surface and on other sample numbers. The standard deviation was calculated and used as $1\sigma$ the results.

The advancing contact angle was measured by placing a $2\mu L$ droplet on the surface while increasing the volume with a rate of $1\mu L/s$. Meanwhile, the contact angle was measured every second until the baseline of the droplet started to increase. After the baseline was measured, the volume was increased by $4\mu L/s$ until a final droplet volume of $5\mu L$. Next, the receding contact angle was measured by decreasing the droplet volume first with a rate of $4\mu L/s$ and was adjusted to $1\mu L/s$s when the baseline was close to receding.

### 3.3.2. Scanning electron microscopy(SEM)

The obtain topological information from the samples, a Field emission-SEM (Hitachi S-4800 FE-SEM ) was used. Images were taken with a beam voltage of 1KeV and a beam current of $1\mu$A. Depending on the samples also, secondary electron suppression was used. The non-conductive polymers were not coated in gold due to the use of a field emission-SEM

### 3.3.3. Atomic force microscopy (AFM)

For surface topology analysis on the nanoscale and to determine surface roughness, AFM(Bruker Dimension Icon) was used. For each sample, there were significant deviations in the softness of the materials and magnitude of elevation. Therefore, different scanning parameters were used for each sample. Amplitude values of 80-150 nV, a feedback gain of 0.05-0.5, and scan rates of 0.6-0.9 Hz were used for the characterization.

### 3.3.4. X-Ray diffraction (XRD)

To analyze the sample's degree of order, XRD was performed using a Bruker D8 advanced diffractometer with a $Cu - K\alpha$ source and a lynxeye-XE-T position-sensitive detector. The diffraction pattern is recorded in the 2θ range from 8◦ to 60◦ with a scanning speed of 0,1 degrees per second.

### 3.3.5. X-Ray Photoelectron Spectroscopy (XPS)

To analyze the chemical composition of the surface, XPS(ThermoFisher Scientific Nexsa) was performed. Firstly, for the samples with a coating, a survey scan was done to obtain information about the top layer of the coating. Secondly, an depth profiling scan was performed, wherewith a repetition of ion-etching and scanning in limited binding energy ranges, shown in Table 3.2, a depth profile was obtained.

**Table 3.2:** Binding energy ranges used to determine atomic percentages of certain elements.

| Element | Orbital | Binding energy range (eV) |
|---|---|---|
| C | 1s | 279 - 294 |
| N | 1s | 392 - 410 |
| O | 1s | 525 - 545 |
| Si | 2p | 95 - 110 |
| Ti | 2p | 448 - 475 |

### 3.3.6. FTIR

The molecular spectrums of both irradiated and non-irradiated materials are measured with a Thermo Nicolet 6700 IR spectrophotometer. The measurement is done in the wavenumber range 500–4000 cm−1, with the air as background.

## 3.4. Mechanical characterization methods

To track the change in the irradiated samples' mechanical properties, a compression test has been done. The samples were placed on the sample holder of a Zwick 20Kn compression bench and were compressed, with a speed of 1mm/sec, up to 15Kn or until the sample fractured.

## 3.5. Radiation sources

For the irradiation of the materials, two radiation sources are used. Firstly, a Gammacell 220 Excel with a Cobalt-60 source inside, with a respective dose rate of 0,566 kGy/h, was used. Inside, the gamma fluence is homogeneous due to the positioning of multiple Co-60 sources surrounding the sample position. The materials were placed inside small polystyrene containers or small glass tubes filled with 1M $HNO_3$ solution. Irradiation times are respectively 17 hours, 7 days, 2,3 months for 10kGy, 100kGy and 1MGy

Secondly, a Van der Graaf electron accelerator was used to irradiate the samples with electrons. Irradiation with a beam current of 208.5 µA beam current and a voltage of 1MeV resulted in an average dose of 48.0 $kGy/cm^2$ in 80 seconds. During the irradiation, the table temperature was monitored not to have exceeded 40 °C. Irradiation rapport can be found in Appendix B

## 3.6. ICP Optical Emission Spectrometry (ICP-OES)

For some of the $NHO_3$ solutions, an ICP-OES analysis was needed to measure the amount of $TiO_2$ in the solution. For this analysis, an ICP (PerkinElmer - Optima 8000) was used to measure the concentration in the solution. Firstly, a reference line was obtained with solutions of which the molarity was known. Therefore, a titanium ICP standard solution(Certipur) was diluted to 0.2, 0.5, and 1 $\mu g/L$. Secondly, the solutions are measured and compared with the values from the standard solutions.

# 4

# Results and discussion

In order to address the research questions, a comprehensive comparison between the different materials and the different conditions must be made. Therefore, multiple different smaller comparisons have been made. However, before comparison between the materials discussed in Chapter 3 can be made, an extensive overview is needed from the pristine materials exposed to 0Gy, 10kGy, 100kGy, and 1MGy, and under the influence of a wet and dry environment. Secondly, a $TiO_2$ thin-film coating is deposited on the materials and evaluated. Next, they are placed in a dry and wet environment under the influence of gamma radiation and compared with each other. As mentioned in section 2 additives could increase the radiation stability of the materials. Therefore, a nano-composite has been made with PDMS, where bentonite clay and PDMS are mixed together to check if this nano-composite could decrease the radiation-induced effects. To validate, if the damage done by gamma irradiation can be compared with $\beta^-$ irradiation, the samples are irradiated under an electron accelerator. Finally, to characterize if the bulk of the material is affected by the radiation and whether a $TiO_2$ thin film coating served as a protective layer. The samples have been compressed and compared with each other.

## 4.1. Pristine material characterization

In this subsection, the pristine materials are evaluated. Therefore, each of them is exposed to different doses of gamma radiation. Radiation exposure can modify the (surface) characteristics due to mechanical and chemical modifications. To see how radiation influences the surface of the material, the wettability is determined with the help of the advancing contact angle. The ACA of several non-modified materials is shown in Figure 4.1. Each material has been irradiated with gamma radiation for respectively 17 hours, 7 days, and 73 days so that a dose of 10kGy, 100kGy, and 1MGy has been delivered. From the figure, it is clear to see that all the polymers follow the same trend. Note that this comparison cannot be made for quartz due to a static contact angle measurement. This was due to a natural hydrophilic surface, which made it challenging to perform the method for ACA measurement discussed in section 2.2. What stands out is the decrease in the advancing contact angle at 10kGy dose for all of the polymers.

Furthermore, after a dose deposition of 100kGy, the hydrophobicity of all the samples increases. Then, it stabilizes and slowly increases when a dose 1MGy is deposited except for PDMS, which decreases its hydrophobicity when the dose increases. It was initially proposed that -the OH group is responsible for decreasing the ACA. For quartz, another trend can be observed the CA rapidly increases while the increment rate lowers over time.

In order to understand the wetting phenomena, there are two directions: the surface functional group and the roughness. These two factors are essential as they can modify the surface characteristics. First, an FT-IR measurement for samples with a dose of 0Gy, 10kGy, and 1 MGy, is done directly after the samples were taken out of the chamber. A confirmation experiment is done after a certain period of time, and no significant change is observed with the FT-IR to see if there is a change of functional groups at the surface. Secondly, the surface roughness of the material is mapped out with an AFM. With the AFM the minimal and maximum peak values are measured and the Ra represents the peak distribution.

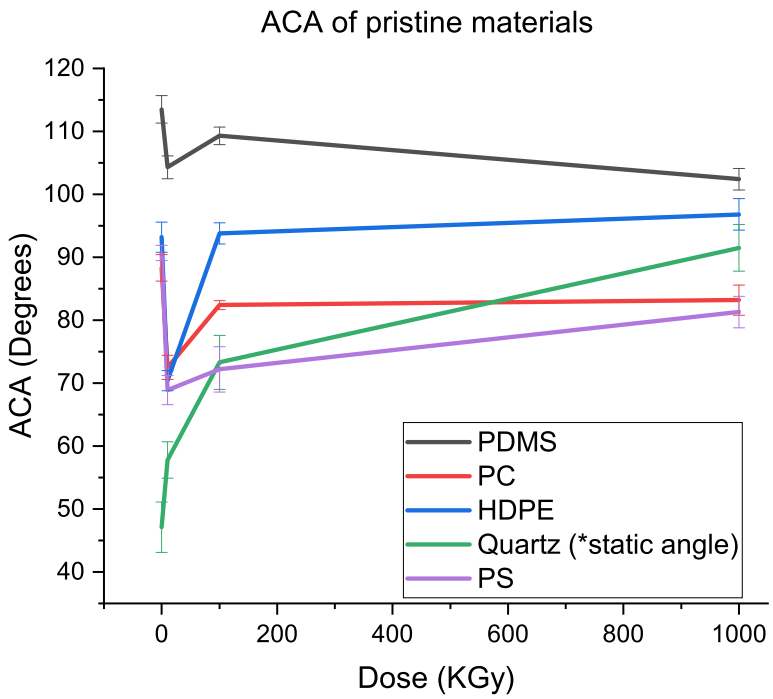


**Figure 4.1:** Advancing contact angle of the pristine materials with 0Gy, 10kGy, 100kGy and 1MGy dose.

**Investigation of surface group and mechanical morphology changes due to gamma radiation**

### 4.1.1. PDMS

Figure 4.2 shows FTIR spectrum of PDMS at 0kGy, 10kGy, and 1MGy. Since the PDMS sample shows a more hydrophilic contact angle at 10kGy, which slowly increases at 100 and decreases again at 1MGy, it was initially proposed that the -OH group is responsible for decreasing the ACA. However, if the peaks in the range of 1300-1800$cm^{-1}$ and 3050-3700$cm^{-1}$ (which indicates OH) is inconclusive. Distortion is found instead of an expected shift in peak or changes in peak intensity. This is due to several reasons: such as contamination or limitation of FTIR equipment. Furthermore, a decrease of the intensity at the peaks at 2963-2905 $cm^{-1}$, characterized by the stretching of the methyl group attached to Si, and $CH_3$ rocking at 785-815$cm^{-1}$ can be observed. This would be expected as an decrease in $CH_3$ stretching would be expected with the hydrophilization of the PDMS surface[51].

Finally, two peaks around 2330$cm^{-1}$ and 2360$cm^{-1}$ can be observed that should not be present in an FT-IR spectrum of PDMS. This can be addressed to the presence of $CO_2$ in the sample. Notable is that the intensity of these peaks decreases when the deposited dose increases, which indicates scission of the C=O bonds[52]. It is hard to conclude what this means for the wettability of PDMS because, under normal conditions, this peak should not be present in PDMS. As the surface wettability is dependent on both the functional groups and surface morphology, a 3D representation of the surface is shown in Figure 4.3a - 4.3d.

PDMS is a hydrophobic material, and the behavior of droplets on the surface can be categorized in the Cassie-Baxter state, as discussed in section 2.2. PDMS becomes less hydrophobic when the dose deposition increases and can be the result of an increased micro-roughness of the surface. Due to the increase in the micro-roughness, the surface tends to behave more like a ”flat” surface, as air is trapped in the nanogaps of the surface. As seen in Figure 4.3a - 4.3d, there is not a change in magnitude of order in the surface roughness. Furhtermore, the Ra value does not show significant change. There is a small decrease in the Ra as the values differ from 2,57nm at 0Gy to 1,22nm at a dose of 1MGy. Due to the small difference its hard to say if the peak distribution influences the wettability.

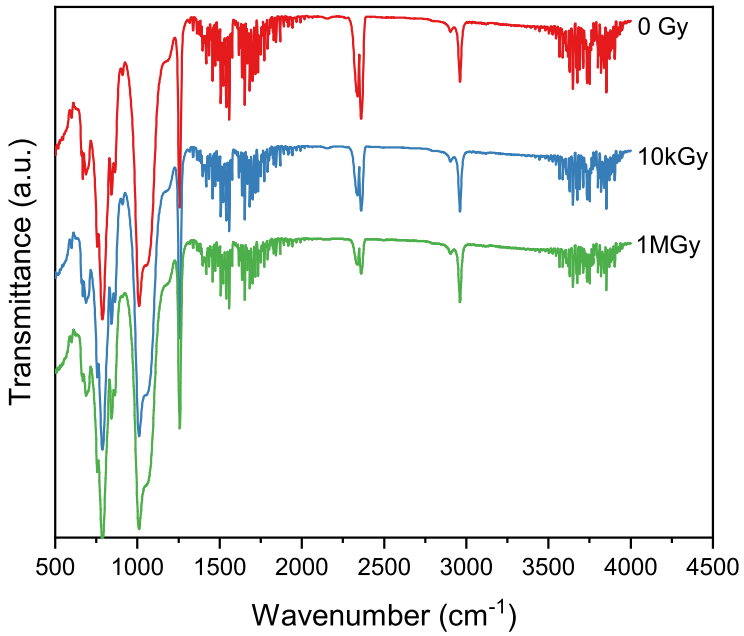


**Figure 4.2:** FTIR of PDMS irradiated with 0Gy, 10kGy and 1MGy

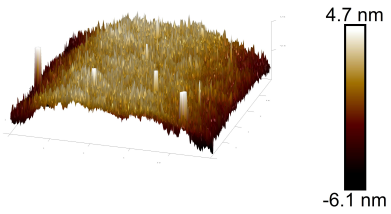


**(a)** 3D representation of the surface of PDMS with 0Gy

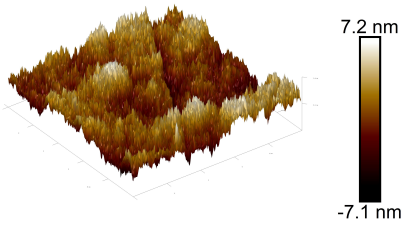


**(b)** 3D representation of the surface of PDMS with 10kGy

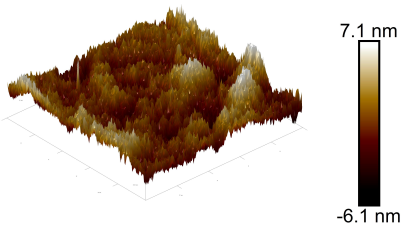


**(c)** 3D representation of the surface of PDMS with 100kGy

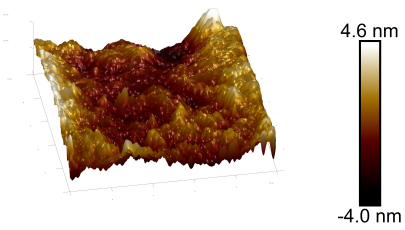


**(d)** 3D representation of the surface of PDMS with 1MGy

**Figure 4.3:** AFM surface analysis from PDMS exposed to different doses

### 4.1.2. HDPE

The wettability of HDPE does not seem to be influenced as the ACA between 0Gy and 1MGy is shown in figure 4.1 does not be significantly different with the exception of the drop in wettability at 10kGy. In figure 4.4, the FT-IR spectrum of the pristine HDPE is shown. What can be observed is the decrease in intensity of the peaks at 2927, 2848, 1460 cm-1, and 700 $cm^{-1}$ when the dose increases. These peaks can be assigned to asymmetric and symmetric stretching of methyl and methylene (–CH2–) groups, C-C stretching, and C=C bending. Without the increase of hydrophilic groups, it is difficult to conclude if the decrease in these groups modifies the surface wettability. As the intensity of the $CH_3$ peaks decreases and with a dose of 1MGy, weak bonds at 1650-1675 cm-1 occur, representing trisubstituted and tetrasubstituted alkene chains. It seems that the irradiated samples form crosslinked bonds from the main chain of the polymer structure[53, 54, 55]. The peak at 1720cm-1, indicative of ketone carbonyl groups, can be explained by the oxidative degradation discussed in section2.1.2[56, 57]. The formation of this group should make the surface more hydrophilic. However, if compared with the ACA in figure 4.1, this is not the case.

According to the AFM images shown in figure 4.5a - 4.5d, the micro-roughness seems to increase as more conical hills can be observed. According to Grubb et al., the crystalline state of PE is affected by gamma irradiation. They assumed that conical hills are created due to deformation of the crystalline sub units[58]. Furthermore, an increase in hills and valleys can be observed. This can be explained by the formation of volatile products during gamma radiation, as discussed in section 2.4. The produced gasses probably force themselves out from the surface, causing the formation of irregular valleys and hills[58]. The expectation would be that these hills and valleys increase the hydrophobicity of the surface, but that seems not to be the case as the FTIR of HDPE showed an increase in the ketone carbonyl for the dose of 1MGy and an increase in the surface roughness. It is plausible that these modifications compensate for each other.

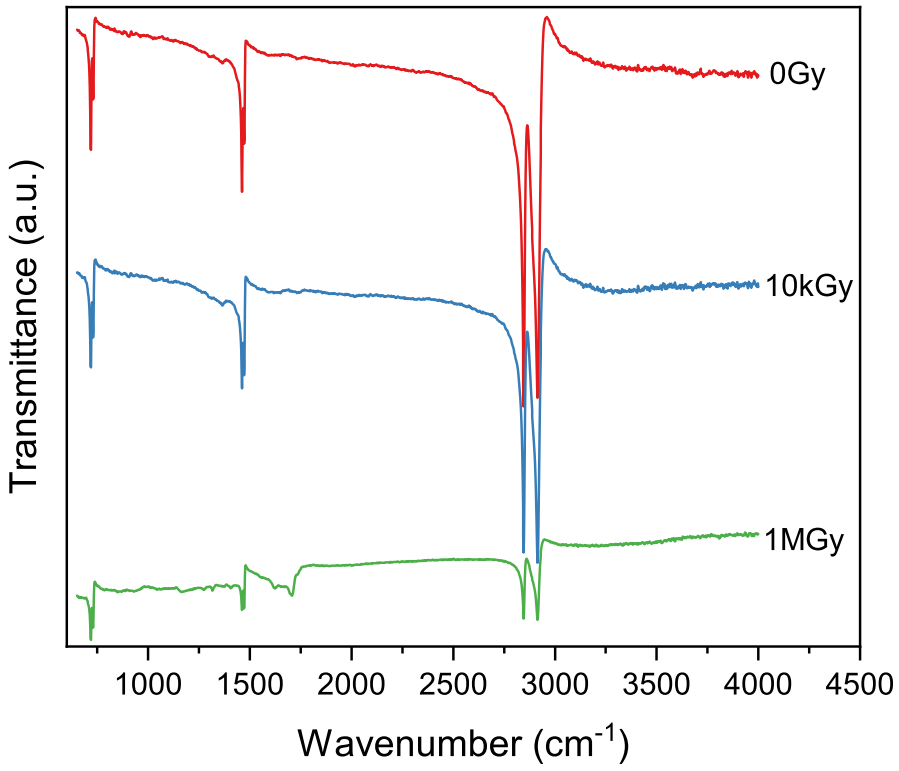


**Figure 4.4:** FT-IR spectrum of pristine HDPE

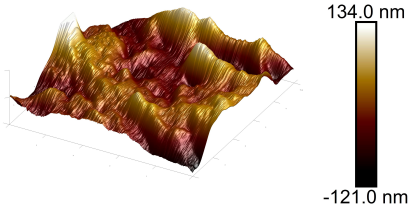


**(a)** 3D representation of the surface of HDPE with 0Gy

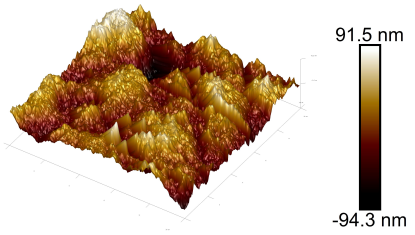


**(b)** 3D representation of the surface of HDPE with 10kGy

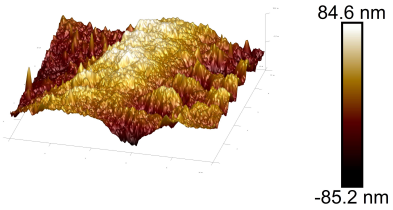


**(c)** 3D representation of the surface of HDPE with 100kGy

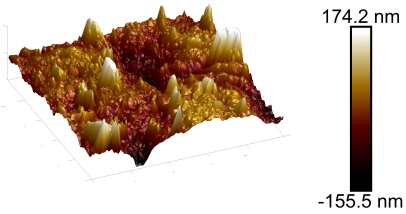


**(d)** 3D representation of the surface of HDPE with 1MGy

**Figure 4.5:** AFM surface analysis from HDPE exposed to different doses

### 4.1.3. PC

The FT-IR spectrum of the pristine PC with and without gamma irradiation is shown in Figure 4.6. It is clear that the intensities for some of the major bonds change due to exposure to gamma radiation. The intensity of peaks corresponding to C−H bonds of CH3 group (2968 $cm^{-1}$ and 2874 $cm^{-1}$), C=O bonds (1725 $cm^{-1}$), aromatic C−O bonds (1434 $cm^{-1}$),C−O−C bonds (1206 $cm^{-1}$), and aromatic C−H bonds (999 $cm^{-1}$) decreases when the deposited dose increases[33, 55]. This indicates that there is scission of these bonds when exposed to radiation, which can lead to an increase in the free radical density and thus the electron density in the sample. According to D. Shina et al., the increase in electron density is the reason for the decrease of the C=O bond order, which results in the decrease of the carbonyl groups[33].

The surface roughness of PC does not seem to change up to a dose of 100kGy, but when a dose of 1 MGy is deposited, there is an irregular formation of protrusions. This can also be addressed to the volatile products created during the irradiation, as discussed above[58]. The roughness seems to increase as the Ra for 0,10 and 100kGy fluctuate around 2nm, and this increases to 6nm at a dose of 1MGy. However, this does not seem to influence the ACA of PC, which should not be expected. The distribution of the peaks increases and this results in an increase of the air pocket size and thus results in rougher surface. There might be a competing effect between surface energy and roughness which cannot be explained with the FTIR used for this study.

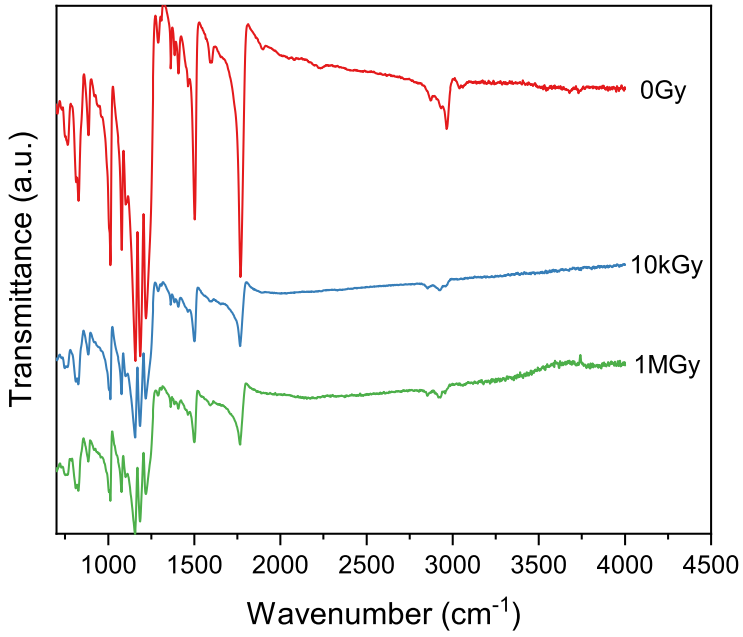


**Figure 4.6:** FT-IR spectrum of pristine PC

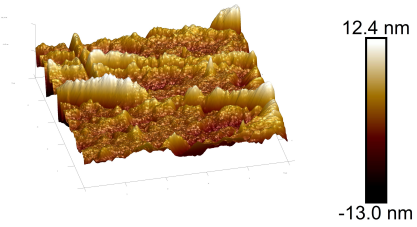


**(a)** 3D representation of the surface of PC with 0Gy

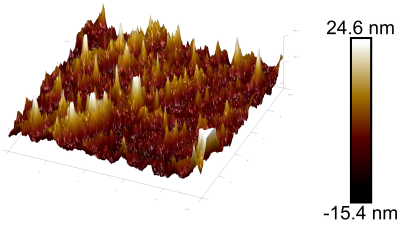


**(b)** 3D representation of the surface of PC with 10kGy

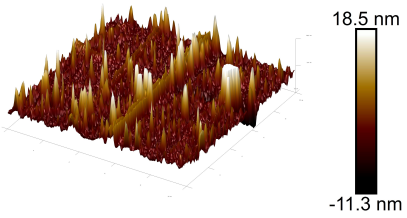


**(c)** 3D representation of the surface of PC with 100kGy

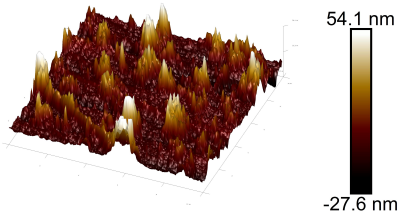


**(d)** 3D representation of the surface of PC with 1MGy

**Figure 4.7:** AFM surface analysis from PC exposed to different doses

### 4.1.4. PS

The molecular structures of both irradiated and non-irradiated polystyrene with gamma irradiation are shown in 4.8. The characteristic peaks at 3100 - 3000 cm−1 correspond to the =C-H stretching due to the aromatic ring. The symmetrical and asymmetrical stretching of $CH_2$ can be addressed to the peaks at 2927 and 2848 cm-1. Peaks at 1602, 1490, and 1447 cm−1 correspond to the stretching vibration of the C=C bond on the aromatic ring. The peak at 1022 cm-1 is the stretching of C-O bonds, and the peak at 903 corresponds to C-H bending[55, 59, 60]. According to the literature discussed in section 2 polymers with aromatic rings tend to be more stable, as they are able to dissipate the incoming energy better. There is also an occurrence of a peak around 1720cm-1 which represents C=O stretching. In the AFM images of PS, shown in Figure 4.9a - 4.9d, a clear trend can be observed where the roughness increases with the increase of the deposited radiation. Due to this trend it is assumable that there is a shift between the Cassie Baxter to Wenzel state. When the surface roughness is compared with the ACA in figure 4.1, after the 10kGy deposition the sample becomes more hydrophobic with the increase of the dose deposition.

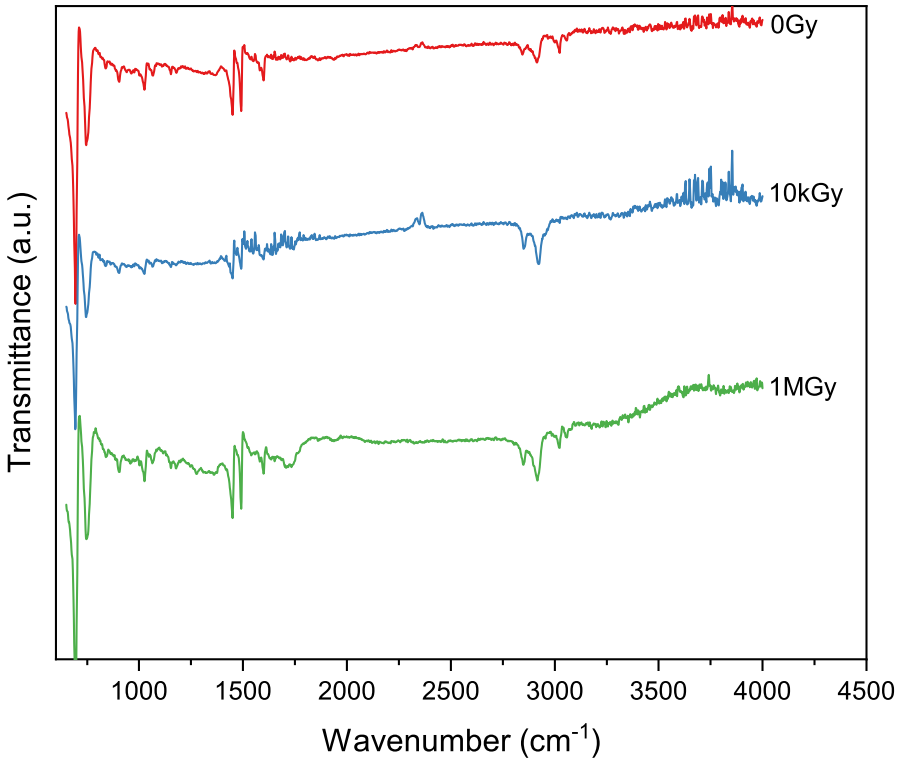


**Figure 4.8:** FT-IR spectrum of pristine PS

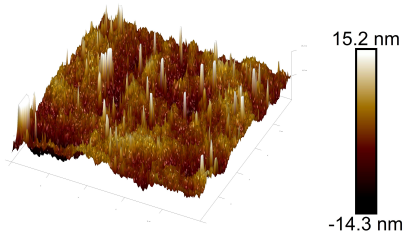


**(a)** 3D representation of the surface of PS with 0Gy

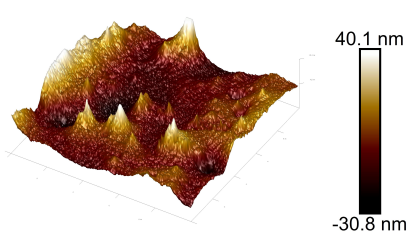


**(b)** 3D representation of the surface of PS with 10kGy

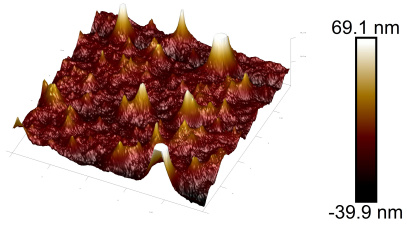


**(c)** 3D representation of the surface of PS with 100kGy

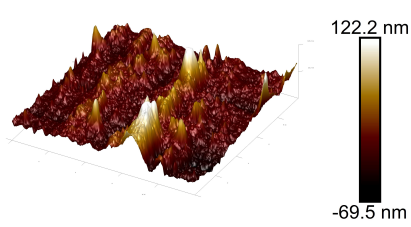


**(d)** 3D representation of the surface of PS with 1MGy

**Figure 4.9:** AFM surface analysis from PS exposed to different doses

### 4.1.5. Quartz

As seen in Figure 4.1, quartz becomes more hydrophobic when exposed to radiation. To validate if this can be addressed to chemical modifications, an FT-IR spectrum of the pristine quartz is shown in 4.10. A few characteristic peaks for quartz were observed. The peak at 780 - 1100 cm−1 was assigned to the different Si-O-Si stretching vibrations. Two peaks that stand out are the peaks at 2920 cm−1 and 2853 cm−1, which are the asymmetric and symmetric $CH_2$ stretching vibrations. These peaks are only present in the sample that is irradiated with 1MGy. In general, it means that $CH_2$ makes the surface less wettable. Furthermore, a better insight into the mechanical morphology is needed to state a conclusion about the increase of hydrophobicity. The surface of quartz can be categorized according to Wenzels' theory. So the increase in hydrophobicity can be addressed to the increase of surface roughness. When image 4.11a and 4.11d are compared with each other, an increase in the order of 100 magnitudes can be observed. This is the result of point defects in the molecule structure of the glass, which cause irradiation-induced oxygen vacancies on the surface[61].

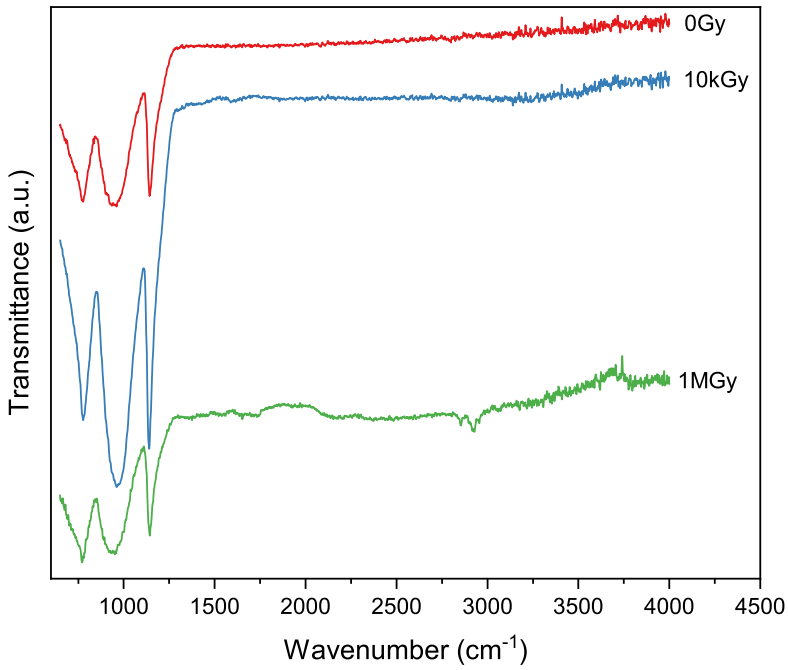


**Figure 4.10:** FT-IR spectrum of pristine quartz

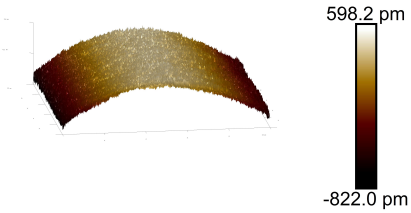


**(a)** 3D representation of the surface of quartz with 0Gy

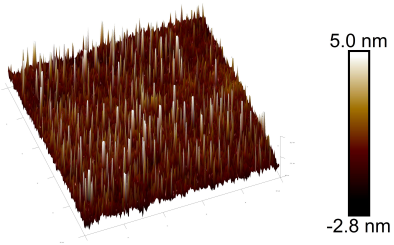


**(b)** 3D representation of the surface of quartz with 10kGy

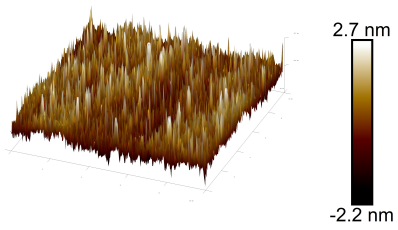


**(c)** 3D representation of the surface of quartz with 100kGy

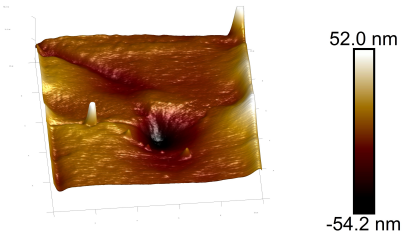


**(d)** 3D representation of the surface of quartz with 1MGy

**Figure 4.11:** AFM surface analysis from quartz exposed to different doses

### 4.1.6. Comparison between the samples

These five materials are often used as microfluidic material, with PDMS and quartz as the most prominent one. In the FTIR spectra, the most changes can be found in the carbon bonds. Nevertheless, the FTIR is not sufficient enough to explain the change in contact angle at 0Gy-10kGy-100kGy. As the used during this research made a spectrum of the whole sample and did not focus on the surface layer of the material where chemical changes are expected. Temporary Radiation-induced surface activation is an interesting phenomenon to look into for the change in wettability. However, this will be discussed in more detail in section4.5. When the results of the FTIR are compared with the ACA in figure 4.1, it is not entirely possible to explain the trends happening there. As mentioned before, exposure to radiation can modify the (surface) characteristics due to mechanical and chemical modifications.

## 4.2. Dry and wet comparison of the pristine samples

In the previous section, an extensive elaboration is given for the pristine materials. However, to get a better understanding of how the materials will behave when used in a microfluidic chip for the LLE of radioisotopes, it is necessary to include a wet and dry comparison between them. In Figure 4.12a - 4.12e the contact angle for each material, with a dose deposition of 0Gy, 10kGy, 100kGy, and 1MGy stored in a wet (1M $HNO_3$) and dry environment is given.

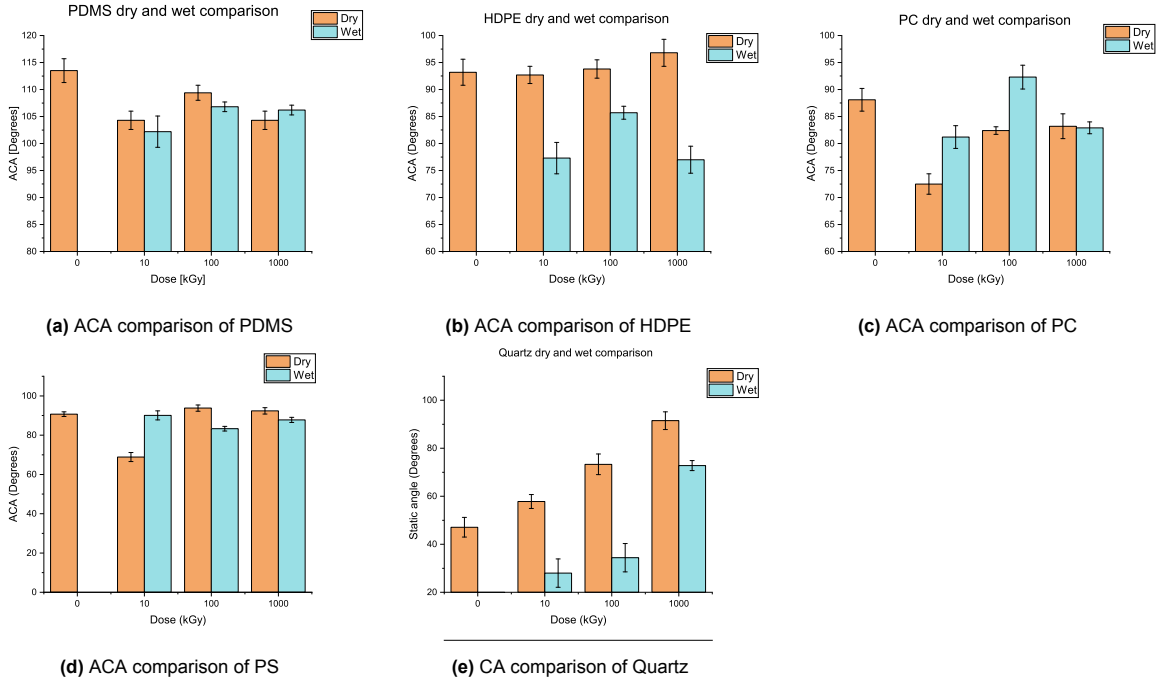


**(a)** ACA comparison of PDMS

**(b)** ACA comparison of HDPE

**(c)** ACA comparison of PC

**(d)** ACA comparison of PS

**(e)** CA comparison of Quartz

**Figure 4.12:** CA comparison of the materials in wet and dry environment with a dose of 0Gy, 10kGy, and 1MGy

### 4.2.1. PDMS

Looking at figure 4.12a, for PDMS, it seems that a wet environment does not significantly influence the wettability of the surface. PDMS is known to be inert against many aqueous solutions and thus resistance against possible oxidation[62]. So it is difficult to say whether the wet environment has an influence on the wettability of the PDMS samples.

### 4.2.2. HDPE

When HDPE in a wet and dry environment is compared in figure 4.12b, a significant difference in the ACA can be observed. The HDPE irradiated in a wet environment is more hydrophilic. When looking at the surface roughness of these samples (shown in additional figures), it seems that the irradiation has a more negligible effect on the surface compared with the samples kept in a dry environment. Accordingly, as stated in the previous section, this should not decrease the ACA as the surface roughness is not

significantly changed. However, looking a bit deeper using XPS in figure A.7, when comparing the C1s XPS spectra of HDPE 10kGy in wet and dry environments are compared, a new peak in the 286eV binding energy can be observed. This can be addressed to the increase of C-O-C groups in the HDPE samples. These ether groups are stated as hydro neutral. However, they can disrupt the hydrophobicity of its neighboring carbon atoms[63].

### 4.2.3. PC

A remarkable difference can be observed between the 10kGy and 100kGy samples for PC, in figure 4.12c. When looking at the AFM images of these two samples, shown in figure A.1, there is not a change in the magnitude of the order of the roughness, and the Ra values of the samples are comparable with each other. So the explanation that there are more air pockets available for the droplet to spread its force to increase the hydrophilicity does not apply here. Therefore, the difference should be in chemical modifications. To prove there are chemical changes at the surface, FTIR or XPS is needed directly after the irradiation. Without these measurements, it is hard to conclude where the difference between wet and dry environment originates.

### 4.2.4. PS

When HDPE in a wet and dry environment is compared in figure 4.12d, there does not seem to be a significant difference between the samples except for the sample irradiated with 10kGy in a dry environment and 100kGy in a wet environment. Both do not show a significant difference in the AFM images. Thus further research with a surface-specific FTIR is needed.

### 4.2.5. Quartz

In the section above, the increase in surface roughness for quartz is already described. However, when the quartz is stored in a wet environment, it seems that quartz becomes more hydrophilic when compared with the quartz stored in a dry environment. This can be addressed to the surface roughness of the quartz, shown in additional figure A.2. For the quartz kept in a wet environment, radiation tends to have less impact on the surface as there is no increase in the order of magnitude of the surface roughness. According to Aines et al., water can enter the structure after a threshold of damage is reached and stabilize the metamict state by annealing local charge imbalance. This means that the crystalline state of the quartz is being preserved [64].

### 4.2.6. Comparison between the samples

In this section, surface modifications are evaluated when the samples are irradiated in a dry or wet environment. While for some samples such as PDMS and PS, little to no change of the wettability can be observed, others experienced significant change. The surface degradation of quartz seems to be slowed down due to the wet environment. This might have to do with the free radicals reacting with the peroxy groups as discussed in 2.1.2, resulting in fewer oxygen vacancies in the sample. The wettability of HDPE is influenced by radiation-induced oxidation.

## 4.3. Characterization of the materials with a $Tio_2$ thin film deposition with vacuum and atmospheric atomic layer deposition

To give more insight into the second objective: if a $TiO_2$ thin film coating can reduce the chemical and mechanical surface modifications of the materials, a coating is deposited on the materials. However, before a clear comparison can be made, the deposition quality must be assessed, and the thickness of each thin film coating deposited with APALD is given in Table 4.1 and the ALD parameters can be found in 3. The thickness of the 700 cycles VALD was only measured on PDMS and resulted in a thickness of 494,56 Å. Furthermore, the wetting property of the coated materials is being assessed within the first 48 hours as the thin film tends to lose a bit of its hydrophilicity[43]. Furthermore, as discussed in section 2.3, the ALD is needed to operate within the temperature window. Unfortunately, this overlapped with the glass-like temperature of PS thus, the deposition on this material was not possible. Therefore, PS is missing in this comparison.

During the deposition of the $TiO_2$ thin-film coating, one of the valves next to the $TiO_2$ bubbler was malfunctioning. This may have resulted in a distortion in the deposition and might influence the thick-

**Table 4.1:** Deposition thickness of the $TiO_2$ thin-film, measured with ellipsometer, on the different materials.

| Material | Cycles | Thickness [Å] | SD | MSE |
|---|---|---|---|---|
| HPDE | 50 | 171,38 | 1,131 | 2,384 |
| PDMS | 50 | 224,49 | 1,624 | 2,964 |
| Quartz | 50 | 140,7 | 0,164 | 0,391 |
| PC | 50 | 130,38 | 0,736 | 1,765 |

ness of the thin film. This must be mentioned because the hydrophobic recovery of samples coated with an APALD $TiO_2$ thin film is quicker than mentioned in other researches[43, 65]. This can be correlated with the out-diffusion of organic species (low molecular weight chains, non-crosslinked polymer chains) or even hydrocarbon adsorption from the ambient atmosphere. It is already known that an infiltration process of the metal oxide into the surface can suppress the apparent hydrophobic recovery[66]. However, in most of our cases, this tends not to happen and might be related due to a malfunction of the ALD. Furthermore, during the ALD, crack formation is inevitable and is assumed to affect the stability of the surface modification. These cracks in the $TiO_2$ thin film may act as pathways for molecules to diffuse to the surface and increase the hydrophobic recovery of the surface[43, 65]. As mentioned above, the ALD is performed in a specific temperature window, and this might result in thermal expansion of the sample and cause buckling of the thin film when cooled down to room temperature.

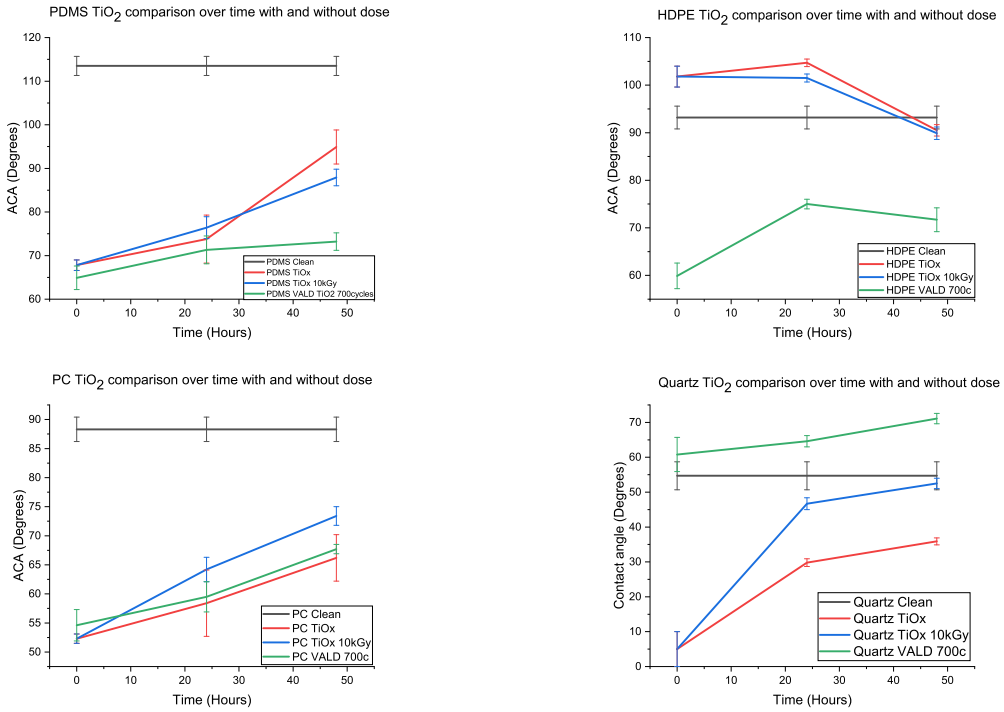


**Figure 4.13:** Advancing contact angle of PDMS, HDPE, PC, and quartz with and without vacuum and atmospheric ALD over the first 48 hours

### 4.3.1. PDMS

The ALD deposition of PDMS is shown in additional figure A.4a. With the SEM images cracks in the coating can be observed. Illustrated in Figure 4.17, the $TiO_2$ thin-film significantly increases the hydrophilicity of the surface of PDMS, as the $TiO_2$ tends to lower the ACA. At 0 hours, the ACA is at its lowest, and within the next 48 hours, the ACA increases slowly, and the surface of the PDMS becomes more hydrophobic. The hydrophobic recovery can be addressed to the out-diffusion of non-crosslinked polymers and is accelerated due to the crack formation in the thin film.

### 4.3.2. HDPE

In theory, the $TiO_2$ thin film should modify the surface to a more hydrophilic state. However, for HDPE coated with the APALD, this is not the case. As mentioned in section 2.3, there is a competition between surface reactions and precursor diffusion into porous substrates such as polymers. A factor that also influences the growth rate of the $TiO_2$ thin film is the number of functional groups available at the surface and their respective density. As HDPE does not have the ideal surface for the nucleation phase of the ALD process, there is island formation of the $TiO_2$ as illustrated in Figures 4.14 and 4.15. Meanwhile, the VALD did not have island formation of the $TiO_2$ thin film as seen in Figure 4.16. This is due to the usage of $O_2$ plasma in the VALD, and this might activate the surface. With the activation of the surface, there is an increase in the number of functional groups, which results in a better nucleation phase during the VALD. This island formation can be the explanation for the increase of the ACA of HDPE coated with the APALD. So at 0 hours the APALD coated samples became more hydrophobic and decreased when the time duration increased. This might has to do with the contamination from the air at the thin film. For the sample exposed with irradiation no significant change could be observed.

**Figure 4.14:** SEM image of APALD coated HDPE at 1K magnification

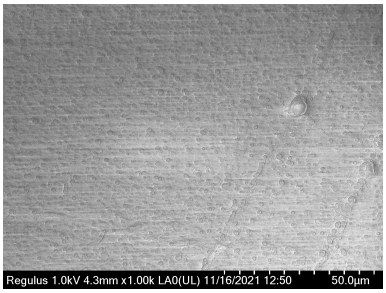


**Figure 4.15:** SEM Image of APALD coated HDPE at 5K magnification

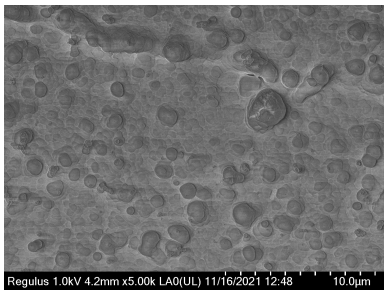


**Figure 4.16:** SEM image of VALD coated HDPE at 1K magnification

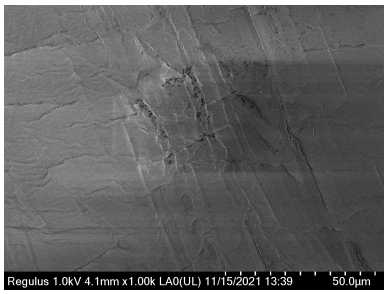


### 4.3.3. PC

PC behaves accordingly to the expectations where the $TiO_2$ thin-film modifies the surface and becomes more hydrophilic. With the SEM image, shown in additional figure A.4c, it is possible to see buckling of the coating and grains are visible. Furthermore, radiation does not seem to influence the recovery in the first 24 hours, but it seems to influence the recovery. However, it is challenging to make a clear statement about this because there is no clear trend when compared with the other samples. So it is difficult to say if radiation plays an essential role in this. It can also be addressed to the change in environment, and thus air quality. This has been tested with a sample kept in the same lab and showed no real difference. However, this still does not exclude the condition of the air inside the gamma cell.

### 4.3.4. Quartz

SEM images of the ALD deposition of quartz is shown in additional figure A.4d. In this figure a clear and uniform deposition can be observed.

The quartz sample that is coated with VALD is, according to the results in Figure 4.17 more hydrophobic, but this can be explained due to the measurement method used for quartz. For the VALD sample, it was possible to measure the ACA, while for quartz coated with the APALD, it was not possible to receive the ACA, and a static contact angle was used. So a comprehensive comparison between these two-sample is challenging to make. It is possible to conclude that the sample treated with APALD was way more hydrophilic during the measurements within the first 24 hours as the droplets of water were pulled from the needle.

### 4.3.5. Effect of VALD and APALD

The recovery rate of the different types of ALD seems not to follow a clear trend. In additional figure A.5, the coating uniformity is shown for the VALD samples and give more insight into the different recovery rate of VALD in comparison with APALD. For PDMS, shown in additional figure A.5a, cracks could also be observed. However, due to the thickness and uniformity of the coating, it seems that

the out-diffusion of PDMS monomers is reduced as the recovery rate is lower. For PC, there seems to be no difference in the recovery rate, while in additional figure A.5c fewer distortions and buckling are observed. HPDE is already discussed in the previous section, and the difference can be explained due to the island formation. For quartz, it is not easy to compare as the way of measurement is different between the samples.

### 4.3.6. Dry and wet comparison with $TiO_2$ thin-film coating

In the previous section, an elaboration of the materials with a $TiO_2$ is given. However, when used in an LLE system, the materials will be in contact with an acid solution. Therefore, it is needed to study the behavior of the coated materials when they are kept in a wet environment. One thing that was directly visible was the color change of the coated materials in a wet environment. The white-ish layer of the $TiO_2$ seemed to be removed from the surface. This was also confirmed with the measured ACA illustrated in Figure 4.17. Where two observations directly stand out. The hydrophobic recovery of PDMS and the increase of hydrophilicity for HDPE in a wet environment. This indicates that the materials recover back to their initial state.

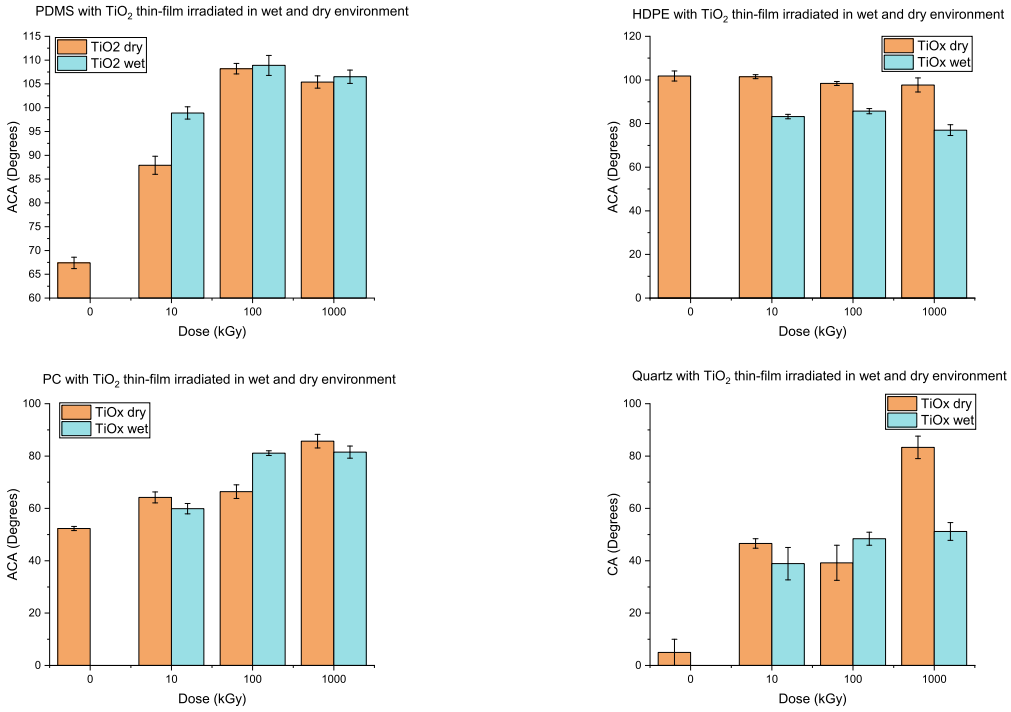


**Figure 4.17:** Water contact angle of PDMS, HDPE, PC, and quartz with $TiO_2$ thin-film deposition stored in dry and wet environment.

That the thin film layer was washed away could be confirmed by the XPS analysis of PDMS illustrated in Figure 4.18. Here it is clearly visible that the Ti compound is significantly reduced on the surface of the sample. A similar graph for HDPE is presented in A.6

However, this gave rise to another question: Did the $TiO_2$ thin-film get washed away due to the $HNO_3$ solution or the exposure to radiation in combination with a wet environment. Therefore, an ICP-OES was performed with four samples of coated PDMS to measure the amount of Ti in the solution. Two of the samples were stored in water and the other two in $HNO_3$, and of both, one was exposed to 10kGy of gamma radiation. The results of the ICP-OES confirmed the expectation that $HNO_3$ was responsible for the removal of the thin film. As in both the $HNO_3$ solution, a concentration of $\sim 8,3 \mu g/L$ was found. while the concentration Ti in the water only resulted in $\sim 0,05 \mu g$/L. It is notable that these quantities are at the lower end of the detection limit

When PC and quartz are compared, there is not a significant change in the (A)CA between the wet and dry environment except for the PC exposed to 100kGy and quartz exposed to 1MGy. As there

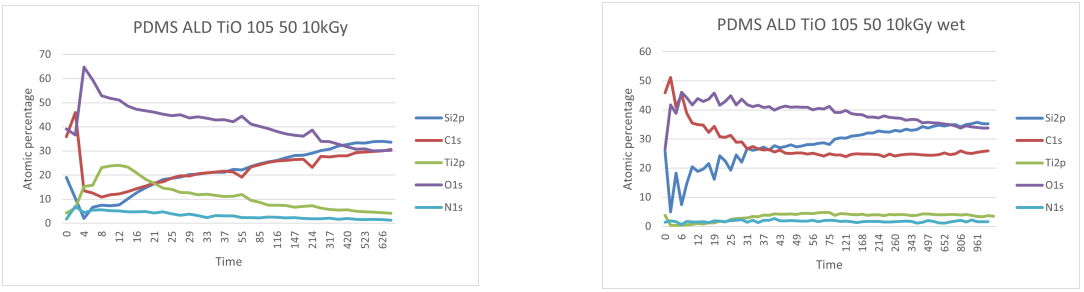


**Figure 4.18:** XPS spectra of PDMS in wet and dry environment after 10kGy exposure from a gamma cell

was little to no difference in the surface roughness, this could not explain the differences, and further research regarding functional groups is needed to make a clear statement and is elaborated in section 5.2

If the ALD coating serves as a protective layer is difficult to say as the time effect of days-month measurement make it inconclusive due to long exposure and result in more chance for contamination. In section 4.5, this time factor is reduced and is the ALD layer re-evaluated.

## 4.4. PDMS with a clay additive

As mentioned in section2.1.2, additives are a way to increase the radiation stability of a material. With the addition of an additive, the material could dissipate the energy of the incoming photons better and should have a better radiation resistance. A study performed by Zhang et al. showed that a composite of styrene-butadiene-styrene/clay improved the radiation resistance of the material[67]. The clay should be able to absorb a large amount of the energy and protect the chains and would produce a large number of free radicals to recombine the chain free radicals of SBS. For this research, a $2wt\%$ PDMS/clay nano-composite was made, and the ACA was compared with pristine PDMS.

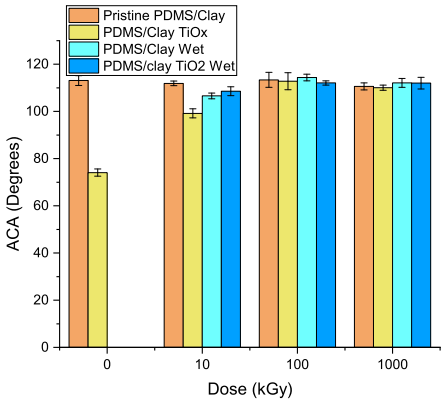


**Figure 4.19:** ACA of PDMS/Clay nanocomposite with(out) coating and stored in dry and wet environment during gamma irradiation

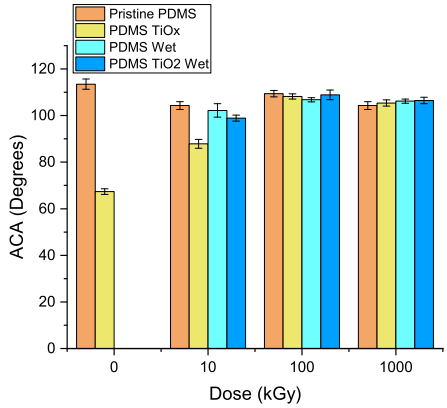


**Figure 4.20:** ACA of PDMS with(out) coating and stored in dry and wet environment during gamma irradiation

As seen in Figure 4.19 - 4.20, there is no significant difference between the ACA of the samples. Thus an assumption can be made that the clay does not influence the behavior of the PDMS at surface level. This can be supported with the fact that surface of PDMS generally relies on the carbon group. For AFM images similar results are expected as both are pourable and follows the mold. However, modifications of the PDMS can be different for the bulk, but this will be elaborated in section 4.6.

## 4.5. Electron irradiation

In section 4.1, a significant increase in the hydrophilicity could be observed for materials irradiated with 10kGy of a low flux Co-60 source. As already stated in the first section, this could probably be addressed to radiation-induced surface activation where hydroxyl groups are temporally bound at the surface of the samples as schematically figured in figure 4.21. Note that the scheme is a simplified version. The purpose of this scheme is to illustrate the interplay of hydrophilic-responsible group (in this case OH-), and hydrophobic-responsible group (in this case CH3-) during and after the exposure. In reality, other molecule and possible (more complex) reaction route also exist.

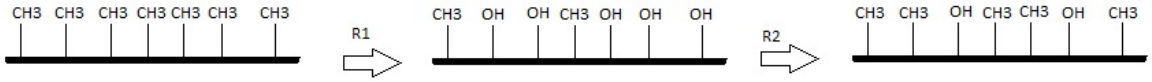


**Figure 4.21:** Schematic representation of risa reaction

In this proposed assumption, there is a constant competition between reaction rate R1 and R2. This reaction rate is influenced by a few things such as initial concentration (of hydroxyl or methyl), exposure with air (or other contaminant), outdiffusion of uncured molecule), provision of energy (due to irradiation), interaction between molecules, porosity (or roughness), and many others. During the low flux irradiation, the reaction rate of R2 is assumed to be predominant over R1. Due to the low flux, long irradiation times were needed to obtain the desired dose and gave the sample more time to recover into its original state. This can occur due to constant exposure with contaminants (air) and outdiffusion of uncured molecule. Furthermore there is a possibility of the polymer to partially recover its initial state as it might be thermodynamically more favourable. Based on all these reasons, the effect of time makes the assessment of the surface energy more complicated.

Therefore, in this section, the samples are irradiated up to 1MGy and 5MGy with a high-flux electron accelerator to eliminate the influences of time-dependent recovery. To achieve 1MGy during the electron irradiation the samples were irradiated for 1 hours in contrast to almost three months for gamma irradiation. Afterwards, the CA was measured and illustrated in Figure 4.22. Please note, due to the APALD capacity, samples coated with VALD are used here.

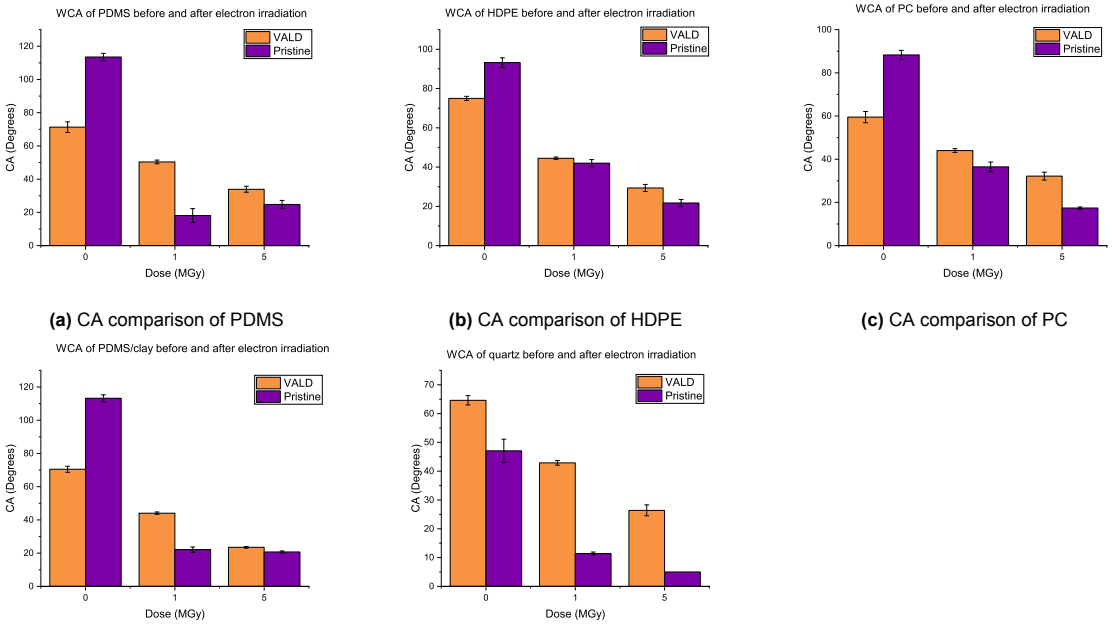


**(a)** CA comparison of PDMS

**(b)** CA comparison of HDPE

**(c)** CA comparison of PC

**(d)** CA comparison of PDMS/clay

**(e)** CA comparison of Quartz

**Figure 4.22:** CA comparison of quartz with and without VALD thin film deposition irradiated with 0Gy, 1MGy, and 5MGy

What directly stands out is the significant change in wettability of all the samples. Radiation-induced surface activation on metal-oxides is an already known principle as discussed in section 2.1.3. However, there is a scarcity of studies involving radiation as a tool for surface modification.

To get a better understanding of the surface change is primarily due to chemical or mechanical modifications, a few AFM and XPS spectra a presented. With the AFM images of PC, HDPE, and quartz shown in additional figure A.3, assumption can be made that the surface roughness did not get affected by the electron irradiation.

As already mentioned in section 4.1, another FT-IR is needed to characterize the functional groups at the surface. However, with the XPS measurements, an assumption can be made to characterize the surface. Due to the destruction of the samples for a mechanical compression test, it was only possible to perform an XPS on PDMS, PC, and quartz with and without VALD. For the pristine PC and quartz, there was a remarkable change in the O1s spectra shown in figure 4.23. If the spectra of PC and quartz are compared with non-irradiated samples found in the literature, a new peak can be observed at 537,3 eV [68, 69]. This peak can be caused by the molecular emission of oxygen in a triple ground state[70]. For PC, there is also a significant increase in the emission spectrum at 289eV, caused by C=O. When the XPS spectra of C1s and O1s of PDMS are observed in figure 4.23, two new peaks can be observed at 535,5eV and 287,3eV both are caused by respectively C=O and O-C=O formation. These functional groups raise the surface energy by replacing the hydrocarbons that cause low surface energy. However, this only produces temporary changes to the surface energy because adsorption of low surface energy molecules will occur over time, slowly reducing the average surface energy.

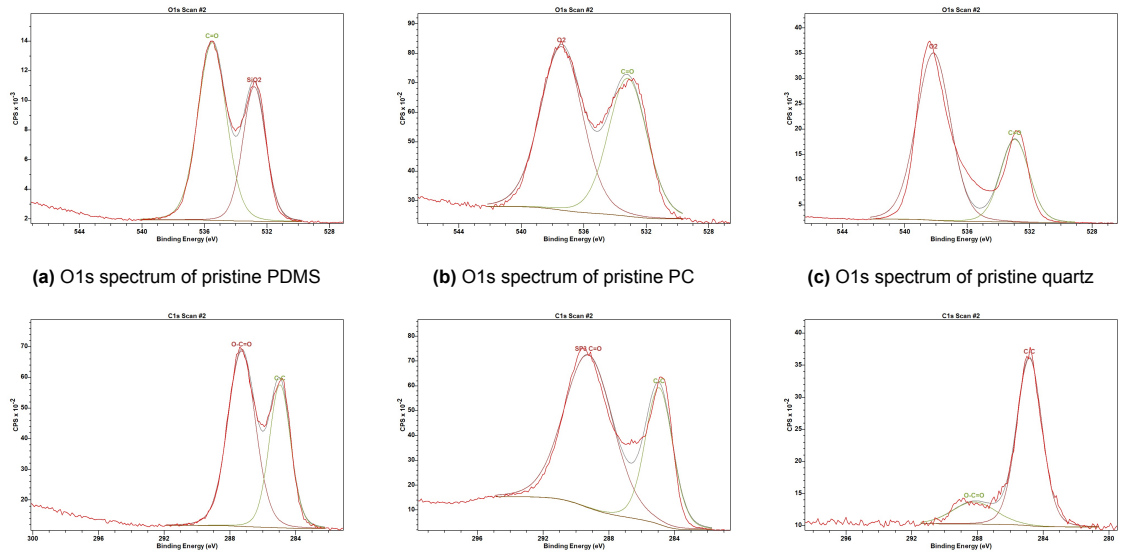

**(a)** O1s spectrum of pristine PDMS **(b)** O1s spectrum of pristine PC **(c)** O1s spectrum of pristine quartz

**(d)** C1s spectrum of pristine PDMS **(e)** C1s spectrum of pristine PC **(f)** C1s spectrum of pristine quartz

**Figure 4.23:** O1s and C1s spectra of PDMS, PC and quartz.

The difference between the VALD and pristine materials can be addressed due to the limited number of oxygen that is present in the $TiO_2$ layer as only one of the two bridging oxygen atoms can bind with a hydroxyl group[33]. Thus restricting the number of hydroxyl bound at the surface.

Radiation induced surface activation is dependent on the surface groups of the samples as each polymer reacts differently on the irradiation. However, if looked at the samples coated with VALD it seems like they follow the same trend and thus stabilizes the surface modification as there are limited binding sites.

## 4.6. Mechanical comparison

In general, most of the radiation-induced modifications can be traced back to changes taking place in the structure of the material. Some of the changes have been attributed to the scission of the polymer chains, promotion of cross-linkages, breaking of covalent bonds, formation of carbon clusters, and liberation of volatile products as discussed in section2.1.2. With these modifications, the mechanical properties of the materials are altered. In this section, the final objective is addressed to check whether the thin film deposition serves as a protective layer for the bulk of the material. Therefore, a comparison, illustrated in figure 4.24, between the samples with and without $TiO_2$ coating has been made, with a dose of 1MGy and 5MGy.

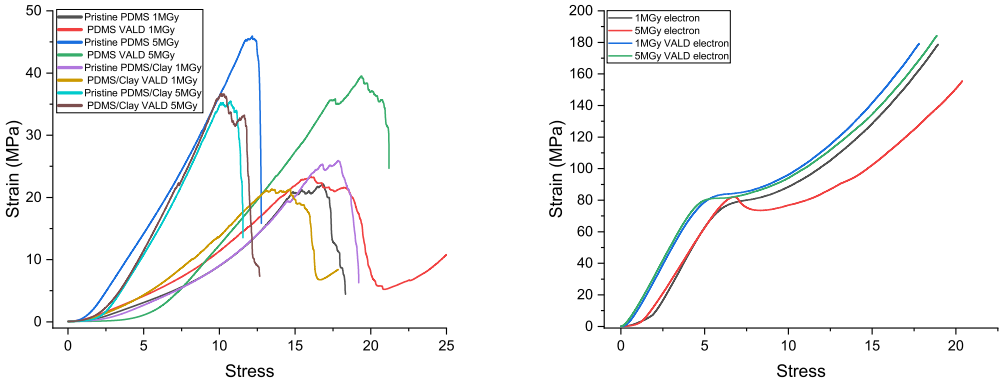


**(a)** Stress and strain curve for PDMS and PDMS/clay

**(b)** Stress and strain curve for PC

**Figure 4.24:** Stress and strain curves

In Figure 4.24a, a comparison is made for the PDMS and the PDMS with a clay additive. An obvious observation is a difference between Young's modulus and the fraction point between the 1MGy and 5MGy samples. It indicates that the samples become more brittle due to crosslinking, as discussed in section 2.1.2. However, if the samples with and without VALD coating are compared, there is not a significant change between Young's modulus and the fraction point of the samples. What also elucidates from this figure is that there is almost no difference between the PDMS and the PDMS with clay. This additive should increase the radiation resistance of the material as it would dissipate the incoming energy better. This might be addressed to the way of bonding of the nano-composite. As Zhang et al. used a chemical way to bond the clay to the polymer string, and in this study, the clay was only mechanically mixed in the solution.

The stress and strain curve of a more impact-resistant polymer, polycarbonate, is shown in figure 4.24b. The samples show a similar Young's modulus, transition zone to plastic deformation, and same rate of densification. Similar results are observed for the other samples as well shown in additional figure 4.24. From this, it is clear to say that the $TiO_2$ thin-film does not serve as a protective layer for the bulk of the material, as it is only a few nanometers thick. This can also be extended to the other types of polymers and quartz, as shown in figure A.11-A.16.

To check if the change in mechanical properties showed above is caused by chain scission or crosslinking of the polymers chains due to radiation, An XRD was performed to get a better insight into the amount of order in the sample and was used by other researchers to shown radiation induced changes[71]. However, XRD is intended to characterize the crystallinity of the materials. Since the materials used in this research are amorphous, they could not be used to make a clear conclusion. Furthermore,the height placement of the samples is crucial and can influence the measurements. Therefore, the XRD spectra are not presented in this study but can be found in Appendix A.5.

# 5

# Conclusion

This experimental research aimed to provide an understanding of the impact of radiation on the materials and how this affects the mechanical properties. In this chapter, the research questions from section1 will be answered. Additionally, some recommendations for future research will be provided.

## 5.1. Conclusion

### 5.1.1. Which material is the most resistant against radiation-induced mechanical and chemical surface modifications after exposure to ionizing radiation.

To answer this question, two factors are essential to consider: The flux and the irradiation in a wet or dry environment.

For low flux gamma radiation, it was clear that the wettability of the polymer surface was less affected by radiation compared to the quartz. Quartz was the only sample where the roughness increased with an order of 100 magnitudes. However, the roughness of PDMS was the least affected by the irradiation.

If looked at the roughness of the high flux irradiated samples, they are comparable with the pristine material. Nevertheless, they show a significant difference in the chemical composition of the surface. All the samples show similar trends. With the XPS, an attempt has been made to analyze the chemical composition of the surface, and an increase in hydroxyl and oxygen groups can be observed, resulting in a hydrophilic surface. However, the rate of recovery of these samples needs to be investigated.

If looked at the mechanical bulk properties of the materials, quartz, polycarbonate, and HDPE showed excellent radiation resistance up to 5MGy. In comparison, PDMS got affected by the radiation and became real brittle.

### 5.1.2. Can a $TiO_2$ thin-film protect the surface of the materials from surface modifications induced by radiation.

A self-limiting $TiO_2$ nanolayer modifies the sample's surface as it is deposited on the surface. The change in wettability is significant. Water contact angle measurements were performed during the first 48 hours to get insight into the hydrophobic recovery rate of the samples due to contamination from the ambient air or short polymers chains that originate from the sample. To minimize this time-dependent effect, high flux irradiation is performed. With this kind of irradiation, the $TiO_2$ coating stabilizes the surface modifications as a clear trend can be observed.

For low flux irradiation, a direct comparison of the functional group at the surface is not possible due to different chemical compositions. However, if looked at the recovery rate of hydrophobicity, there is no clear trend visible. It would be expected that due to irradiation, there is an increase of small polymer strings that diffuses out of the bulk and contaminate the $TiO_2$ coating. However, this is not happening in PDMS. PC and quartz have a more uniform deposition without less crack formation. They are more dependent on the ambient air recovery, which tends to be higher for the irradiated samples. It would be assumable that different reactions occur when there is a different surface composition. However,

without a better chemical composition analysis, it is hard to make a clear statement that the $TiO_2$ coating protects the material's surface.

### 5.1.3. Does the $TiO_2$ thin-film serve as a protective layer for the bulk of the material.

In general, most radiation-induced modifications can be traced back to changes taking place in the structure of the material. Some of the changes have been attributed to the scission of the polymer chains, promotion of cross-linkages, breaking of covalent bonds, formation of carbon clusters, and liberation of volatile products. As seen in section 4.6, there was not a significant difference between the sample with and without a $TiO_2$ coating. The thin film layer is only 40 nm thick, and the range of electrons and gamma radiation is many times higher. Therefore, a conclusion can be made that the thin film deposition by the ALD does not serve as a protective layer to decrease the damage induced by the radiation in the bulk of the material.

## 5.2. Recommendations

Additional research is needed to provide a better insight into the mechanism occurring due to irradiation. Therefore, recommendations are listed below:

1. As stated in section 4.1, the FTIR used during this research was not sensitive enough to measure changes at the surface as the FTIR made a spectrum through the whole sample. Therefore, to better understand the mechanics for the functional groups attached to the surface during irradiation, precise spectra of only the surface are needed.
2. High flux irradiation of materials leads to radiation-induced surface activation and changes the wettability. However, the mechanisms are taking place during the irradiation. Therefore, it is necessary to investigate the behavior of the droplet on the surface during irradiation as, during the separation of radioisotopes, the surface mechanics gets modified. To investigate this, in situ irradiation is needed to better understand how the wettability changes. This can be done by measuring the water contact angle of a droplet placed on the surface while irradiating it with, i.e., a Roentgen tube.
3. During this experimental study, the interactions of gamma photons and electrons are studied. These waves and particles are relatively small when compared with alpha particles. However, their mass is respectively high, which means that their main free path is low and thus result in very little penetration when compared to gamma and beta irradiation. Nevertheless, they have a high linear energy transfer, which results in a greater interaction volume with the material.
4. When the samples with $TiO_2$ thin-film are stored in a 1M $HNO_3$ solution, the coating is rinsed off the surface. As the $TiO_2$ coating tends not to be compatible with an acidic solution, another type of coating is needed to prevent this from happening. One coatings that might have better compatibility with an acidic solution is $SiO_2$ and might be more suited to prevent the surface modification induced by radiation of the materials.
5. Due to high flux irradiation, there was a significant change in the surface's wettability. This should be a temporary modification as carbon in ambient air would contaminate the surface and recover it to its initial state. A preliminarty test after three weeks showed a positive indication. However, the rate of recovery needs to be investigated.

# References


[1] *Cancer*. URL: https://www.who.int/health-topics/cancer#tab=tab_1 (visited on 07/19/2021).

[2] Davide Ciceri, Jilska M. Perera, and Geoffrey W. Stevens. "The use of microfluidic devices in solvent extraction". In: *Journal of Chemical Technology and Biotechnology* 89.6 (2014), pp. 771–786. ISSN: 10974660. DOI: 10.1002/jctb.4318.

[3] Karla Anne Knapp, Michael L. Nickels, and H. Charles Manning. "The Current Role of Microfluidics in Radiofluorination Chemistry". In: *Molecular Imaging and Biology* 22.3 (2020), pp. 463–475. ISSN: 18602002. DOI: 10.1007/s11307-019-01414-6.

[4] N. Assmann, A. Ladosz, and P. Rudolf von Rohr. "Continuous Micro Liquid-Liquid Extraction". In: *Chemical Engineering and Technology* 36.6 (2013), pp. 921–936. ISSN: 09307516. DOI: 10.1002/ceat.201200557.

[5] Sachit Goyal et al. "Thiolene and SIFEL-based microfluidic platforms for liquid-liquid extraction". In: *Sensors and Actuators, B: Chemical* 190 (2014), pp. 634–644. ISSN: 09254005. DOI: 10.1016/j.snb.2013.09.065. URL: /pmc/articles/PMC4167834/%20/pmc/articles/PMC4167834/?report=abstract%20https://www.ncbi.nlm.nih.gov/pmc/articles/PMC4167834/.

[6] Kangning Ren, Jianhua Zhou, and Hongkai Wu. "Materials for Microfluidic Chip Fabrication". In: 46.11 (2013).

[7] A J Timmermans. "Interface stabilization and pinning in parallel liquid-liquid microfluidics using phaseguides and surface roughness". In: ().

[8] O Van Batenburg. "Microfluidic Liquid-Liquid Extraction for Radioiso- tope Separation". In: ().

[9] Rob Wenmaekers. "The use of microfluidics for the purification of medical radioisotopes". In: *Master Thesis* (2018), pp. 1–59.

[10] Bobby R. Scott and Raymond A. Guilmette. "Radiation Toxicology, Ionizing and Nonionizing". In: *Encyclopedia of Toxicology* (Jan. 2005), pp. 601–615. DOI: 10.1016/B0-12-369400-0/00828-0.

[11] *European Radiation Protection Course: Basics - Philippe Massiot, Christine Jimonet - Google Boeken*. URL: https://books.google.nl/books?hl=nl&lr=&id=o2n0AwAAQBAJ&oi=fnd&pg=PR1&dq=Massiot+Philippe+2014&ots=-4zG_iDPZV&sig=NBXTcxmH0FZuBvYbG-0mpxCnJ_c#v=onepage&q=Massiot%20Philippe%202014&f=false (visited on 10/15/2021).

[12] Christian W. Fabjan and Schopper Herwig. *Particle Physics Reference Library Volume 2: Detectors for Particles and Radiation*. Vol. 2. 2020. ISBN: 9783030353179.

[13] Claude Leroy and Pier Giorgio Rancoita. *Principles of radiation interaction in matter and detection, third edition*. World Scientific Publishing Co., Jan. 2011, pp. 1–1018. ISBN: 9789814360524. DOI: 10.1142/8200. URL: https://www.worldscientific.com/worldscibooks/10.1142/8200.

[14] Steven A. Czyz and Abi T. Farsoni. "A radioxenon detection system using CdZnTe, an array of SiPMs, and a plastic scintillator". In: *Journal of Radioanalytical and Nuclear Chemistry* 313.1 (2017), pp. 131–140. ISSN: 15882780. DOI: 10.1007/s10967-017-5287-x.

[15] P. Vivek Vardhan and Lata Israni Shukla. "Ft-ir investigations on effect of high doses of gamma radiationinduced damage to polystyrene and mechanism of formation of radiolysis products". In: *Radiation and Environmental Biophysics* 57.3 (Aug. 2018), pp. 301–310. ISSN: 14322099. DOI: 10.1007/s00411-018-0740-y. URL: https://doi.org/10.1007/s00411-018-0740-y.

[16] D. J. Carlsson and S. Chmela. "Polymers and High-Energy Irradiation: Degradation and Stabilization". In: *Mechanisms of Polymer Degradation and Stabilisation* (1990), pp. 109–133. DOI: 10.1007/978-94-011-3838-3_4.

[17] A. Chapiro. "General consideration of the radiation chemistry of polymers". In: *Nuclear Inst. and Methods in Physics Research, B* 105.1-4 (1995), pp. 5–7. ISSN: 0168583X. DOI: 10.1016/0168-583X(95)00861-6.

[18] J. Davenas et al. “Stability of polymers under ionising radiation: The many faces of radiation interactions with polymers”. In: *Nuclear Instruments and Methods in Physics Research, Section B: Beam Interactions with Materials and Atoms* 191.1-4 (2002), pp. 653–661. ISSN: 0168583X. DOI: 10.1016/S0168-583X(02)00628-6.

[19] Gregory Von White et al. “An Overview of Basic Radiation Effects on Polymers”. In: (2013), pp. 1–35.

[20] Gregory Von White and Rajan Tandon. *An Overview of Basic Radiation Effects on Polymers and Glasses*. URL: https://www.osti.gov/servlets/purl/1671997 (visited on 06/15/2021).

[21] David J. T. Hill and Andrew K. Whittaker. *Radiation Chemistry of Polymers*. 2016, pp. 1–58. ISBN: 0471440264. DOI: 10.1002/0471440264.pst488.pub2.

[22] George Wypych. “PRINCIPLES OF DEGRADATION BY $\gamma$-RADIATION”. In: *PVC Degradation and Stabilization* (2015), pp. 205–213. DOI: 10.1016/B978-1-895198-85-0.50008-X.

[23] Jan F. Rabek. “Chapter 4 Oxidative Degradation of Polymers”. In: *Comprehensive Chemical Kinetics* 14.C (1975), pp. 425–538. ISSN: 00698040. DOI: 10.1016/S0069-8040(08)70336-4.

[24] Shigehiko Tabuse et al. “Radiation protection effects by addition of aromatic compounds to n-dodecane”. In: *Radiation Physics and Chemistry* 62.1 (2001), pp. 179–187. ISSN: 0969806X. DOI: 10.1016/S0969-806X(01)00436-4.

[25] Vijay Kumar. *Radiation Effects in Polymeric Materials*. Vol. 1. 1. 2019. ISBN: 9783030057695. DOI: https://doi.org/10.1007/978-3-030-05770-1.

[26] A. Charlesby. *Charlesby, A 1981 Crosslinking and degradation of polymers.pdf*. 1981. DOI: 0146-5724181/070059-08502.00/0.

[27] Yongxia Sun and Andrzej G Chmielewski. “APPLICATIONS OF IONIZING RADIATION IN MATERIALS PROCESSING edited by”. In: (). URL: www.ichtj.waw.pl.

[28] B.J. Lyons and F.E. Weir. *The Effect of Radiation on the Mechanical Properties of Polymers*. ACADEMIC PRESS, INC., 1973, pp. 281–306. DOI: 10.1016/b978-0-12-219802-1.50021-6. URL: http://dx.doi.org/10.1016/B978-0-12-219802-1.50021-6.

[29] EM Kornacka. “Radiation-Induced Oxidation of Polymers”. In: *Applications of Ionizing Radiation in Materials Processing* 1 (2017), pp. 183–192. URL: http://www.ichtj.waw.pl/ichtj/publ/monogr/sun2017/sun-vol1.pdf#page=184.

[30] L.A. Wall Brown and D. W. “The Journal of”. In: 95.11 (1991), pp. 4173–4176.

[31] R.A. JOHNSON. “Physics of Radiation Effects in Crystals, Volume 13”. In: *Modern Problems in Condensed Matter Sciences* (1992), pp. v–vii. URL: https://linkinghub.elsevier.com/retrieve/pii/B978044489637750003X.

[32] Linn W. Hobbs et al. “Radiation effects in ceramics”. In: *Journal of Nuclear Materials* 216.C (1994), pp. 291–321. ISSN: 00223115. DOI: 10.1016/0022-3115(94)90017-5.

[33] Yoshio HONJO et al. “Mechanism of Hydrophilicity by Radiation-Induced Surface Activation”. In: *Journal of Power and Energy Systems* 3.1 (2009), pp. 216–227. ISSN: 1881-3062. DOI: 10.1299/jpes.3.216.

[34] George Zografi and Barbara A Johnson. “Effects of surface roughness on advancing and receding contact angles *”. In: 22 (1984), pp. 159–176.

[35] Tommi Huhtamäki et al. “Surface-wetting characterization using contact-angle measurements”. In: *Nature Protocols* 13.7 (2018), pp. 1521–1538. ISSN: 17502799. DOI: 10.1038/s41596-018-0003-z. URL: http://dx.doi.org/10.1038/s41596-018-0003-z.

[36] Juuso T Korhonen et al. “Reliable Measurement of the Receding Contact Angle”. In: (2013).

[37] Kai Liu et al. “Tricky contact angle imaging”. In: *Science* 363.6432 (2019), pp. 1147–1148.

[38] Al de Leon and Rigoberto C. Advincula. “Conducting Polymers with Superhydrophobic Effects as Anticorrosion Coating”. In: *Intelligent Coatings for Corrosion Control* (Jan. 2015), pp. 409–430. DOI: 10.1016/B978-0-12-411467-8.00011-8.

[39] Alonso Frank M. *(PDF) Functionalization of Steels and other Metallic Materials with Hydrophobic Layers - Influence on Wetting and Corrosion Resistance*. 2017. URL: https://www.researchgate.net/publication/322627227_Functionalization_of_Steels_and_other_Metallic_Ma

terials_with_Hydrophobic_Layers_-_Influence_on_Wetting_and_Corrosion_Resistance (visited on 07/23/2021).

[40] H. Van Bui, F. Grillo, and J. R. Van Ommen. “Atomic and molecular layer deposition: off the beaten track”. In: *Chemical Communications* 53.1 (2017), pp. 45–71. ISSN: 1364548X. DOI: 10.1039/c6cc05568k. URL: http://dx.doi.org/10.1039/C6CC05568K.

[41] Richard W. Johnson, Adam Hultqvist, and Stacey F. Bent. “A brief review of atomic layer deposition: From fundamentals to applications”. In: *Materials Today* 17.5 (2014), pp. 236–246. ISSN: 13697021. DOI: 10.1016/j.mattod.2014.04.026. URL: http://dx.doi.org/10.1016/j.mattod.2014.04.026.

[42] Steven M. George. “Atomic layer deposition: An overview”. In: *Chemical Reviews* 110.1 (2010), pp. 111–131. ISSN: 00092665. DOI: 10.1021/cr900056b.

[43] Bart van den Berg. “The stability of surface wettability modification on polydimethylsiloxane by atomic layer deposition of TiO”. In: (2021).

[44] Tommi O. Kääriäinen et al. “Atomic layer deposition on polymer based flexible packaging materials: Growth characteristics and diffusion barrier properties”. In: *Thin Solid Films* 519.10 (Mar. 2011), pp. 3146–3154. ISSN: 0040-6090. DOI: 10.1016/J.TSF.2010.12.171.

[45] Gregory N. Parsons et al. “Mechanisms and reactions during atomic layer deposition on polymers”. In: *Coordination Chemistry Reviews* 257.23-24 (Dec. 2013), pp. 3323–3331. ISSN: 0010-8545. DOI: 10.1016/J.CCR.2013.07.001.

[46] *CROW*. URL: https://www.polymerdatabase.com/ (visited on 08/01/2021).

[47] Tatiana Trantidou et al. “Hydrophilic surface modification of pdms for droplet microfluidics using a simple, quick, and robust method via pva deposition”. In: *Microsystems and Nanoengineering* 3.April 2016 (2017). ISSN: 20557434. DOI: 10.1038/micronano.2016.91.

[48] B.K. Gale et al. *Low-Cost MEMS Technologies*. July 2015. 2016, pp. 1–32. ISBN: 9780128035818. DOI: 10.1016/b978-0-12-803581-8.00530-0.

[49] A. A. Miller. “Radiation Chemistry of Polydimethylsiloxane. I. Crosslinking and Gas Yields”. In: *Journal of the American Chemical Society* 82.14 (1960), pp. 3519–3523. ISSN: 15205126. DOI: 10.1021/ja01499a011.

[50] J. H. O’Donnell et al. “CROSSLINKING AND SCISSION YIELDS FOR POLYSTYRENE SUBJECTED TO gamma IRRADIATION IN VACUO.” In: *Journal of polymer science. Part A-1, Polymer chemistry* 17.12 (1979), pp. 4081–4088. ISSN: 0449296X. DOI: 10.1002/pol.1979.170171227.

[51] Debashis Maji, S K Lahiri, and Soumen Das. “Study of hydrophilicity and stability of chemically modified PDMS surface using piranha and KOH solution”. In: (). DOI: 10.1002/sia.3770.

[52] Thomas Schädle, Bobby Pejcic, and Boris Mizaikoff. “Monitoring dissolved carbon dioxide and methane in brine environments at high pressure using IR-ATR spectroscopy”. In: *Analytical Methods* 8.4 (Jan. 2016), pp. 756–762. ISSN: 1759-9679. DOI: 10.1039/C5AY02744F. URL: https://pubs.rsc.org/en/content/articlehtml/2016/ay/c5ay02744f%20https://pubs.rsc.org/en/content/articlelanding/2016/ay/c5ay02744f.

[53] C. Uma Maheswari et al. “A Comparative Study of Modified and Unmodified High-Density Polyethylene/Borassus Fiber Composites”. In: *http://dx.doi.org/10.1080/1023666X.2013.814027* 18.6 (Aug. 2013), pp. 439–450. ISSN: 1023666X. DOI: 10.1080/1023666X.2013.814027. URL: https://www.tandfonline.com/doi/abs/10.1080/1023666X.2013.814027.

[54] A. Sadighzadeh et al. “Characterization of Gamma Irradiated Low and High Density Polyethylene Using the FTIR and DSC Technique”. In: *Journal of Inorganic and Organometallic Polymers and Materials* 25.6 (Nov. 2015), pp. 1448–1455. ISSN: 15741451. DOI: 10.1007/S10904-015-0258-6/FIGURES/10. URL: https://link.springer.com/article/10.1007/s10904-015-0258-6.

[55] *IR Spectrum Table*. URL: https://www.sigmaaldrich.com/NL/en/technical-documents/technical-article/analytical-chemistry/photometry-and-reflectometry/ir-spectrum-table (visited on 01/05/2022).

[56] C. Albano et al. “Effect of gamma irradiation on HDPE/HA (80:20) composites”. In: *Polymers for Advanced Technologies* 16.2-3 (Feb. 2005), pp. 283–285. ISSN: 10427147. DOI: 10.1002/PAT.580.

[57] Hanan Al-Ghamdi et al. “FTIR study of gamma and electron irradiated high-density polyethylene for high dose measurements”. In: *Nuclear Engineering and Technology* 54.1 (Jan. 2022), pp. 255–261. ISSN: 2234358X. DOI: 10.1016/J.NET.2021.07.023. URL: https://doi.org/10.1016/j.net.2021.07.023.

[58] Olgun Güven, Ali Alacakir, and Erdal Tan. “An atomic force microscopic study of the surfaces of polyethylene and polycarbonate films irradiated with gamma rays”. In: *Radiation Physics and Chemistry* 50.2 (1997), pp. 165–170. ISSN: 0969806X. DOI: 10.1016/S0969-806X(97)00002-9.

[59] Jibrin Alhaji Yabagi et al. “The effect of gamma irradiation on chemical, morphology and optical properties of polystyrene nanosphere at various exposure time”. In: (). DOI: 10.1088/1757-899X/298/1/012004.

[60] Junfei Fang, Yimin Xuan, and Qiang Li. “Preparation of polystyrene spheres in different particle sizes and assembly of the PS colloidal crystals”. In: *Science China Technological Sciences* 53.11 (Nov. 2010), pp. 3088–3093. ISSN: 16747321. DOI: 10.1007/S11431-010-4110-5. URL: https://www.researchgate.net/publication/241036546_Preparation_of_polystyrene_spheres_in_different_particle_sizes_and_assembly_of_the_PS_colloidal_crystals.

[61] William J Weber et al. “Waste and Plutonium Disposition”. In: *Journal of Materials Research* 12.8 (1997), pp. 1946–1978. ISSN: 1523-0864.

[62] B.K. Gale et al. “Low-Cost MEMS Technologies”. In: *Reference Module in Materials Science and Materials Engineering* (Jan. 2016). DOI: 10.1016/B978-0-12-803581-8.00530-0.

[63] Fredric M Menger and Mary E Chlebowski. “Is the Ether Group Hydrophilic or Hydrophobic?” In: (2005). DOI: 10.1021/la040113m.

[64] Roger D. Aines and George R. Rossman. “Relationships between radiation damage and trace water in zircon, quartz, and topaz”. In: (1986). ISSN: 0003-004X. URL: https://resolver.caltech.edu/CaltechAUTHORS:20130429-112411934.

[65] Joseph C. Spagnola, Bo Gong, and Gregory N. Parsons. “Surface texture and wetting stability of polydimethylsiloxane coated with aluminum oxide at low temperature by atomic layer deposition”. In: *Journal of Vacuum Science Technology A: Vacuum, Surfaces, and Films* 28.6 (Sept. 2010), p. 1330. ISSN: 0734-2101. DOI: 10.1116/1.3488604. URL: https://avs.scitation.org/doi/abs/10.1116/1.3488604.

[66] Sarah Hashemi Astaneh et al. “Surface and subsurface film growth of titanium dioxide on polydimethylsiloxane by atomic layer deposition”. In: *Applied Surface Science* 493.March (2019), pp. 779–786. ISSN: 01694332. DOI: 10.1016/j.apsusc.2019.07.029. URL: https://doi.org/10.1016/j.apsusc.2019.07.029.

[67] Wei’an Zhang et al. “A novel property of styrene – butadiene – styrene /clay nanocomposites: radiation resistance”. In: *Journal of Materials Chemistry* 14.2 (Jan. 2004), pp. 209–213. ISSN: 09599428. DOI: 10.1039/B307978C. URL: https://pubs.rsc.org/en/content/articlehtml/2004/jm/b307978c%20https://pubs.rsc.org/en/content/articlelanding/2004/jm/b307978c.

[68] John M. Lannon and Qingru Meng. “Analysis of Polycarbonate (PC) by XPS”. In: *Surface Science Spectra* 6.2 (1999), pp. 75–78. ISSN: 1055-5269. DOI: 10.1116/1.1247901.

[69] Stephen M. Francis, W. Edryd Stephens, and Neville V. Richardson. “X-ray photoelectron and infrared spectroscopies of quartz samples of contrasting toxicity”. In: *Environmental Health: A Global Access Science Source* 8.SUPPL. 1 (2009). ISSN: 1476069X. DOI: 10.1186/1476-069X-8-S1-S4.

[70] G. H. Kroll et al. “Interaction of O2 with C60: photon-induced oxidation”. In: *Chemical Physics Letters* 181.2-3 (1991), pp. 112–116. ISSN: 00092614. DOI: 10.1016/0009-2614(91)90341-6.

[71] David Manas, Jozef Dobransky, and Lenka Chvatalova. “Ultra nano-hardness of surface layer of irradiated high-density polyethylene (HDPE)”. In: *MATEC Web of Conferences* 125 (2017), pp. 1–5. ISSN: 2261236X. DOI: 10.1051/matecconf/201712502044.

[72] P. G. Zambonin and E. Desimoni. “X-Ray Photoelectron Spectroscopy: Principles, Instrumentation, Data Processing and Molten Salt Applications”. In: *Molten Salt Chemistry* (1987), pp. 425–445. DOI: 10.1007/978-94-009-3863-2_21.

[73] Deena Titus, E. James Jebaseelan Samuel, and Selvaraj Mohana Roopan. “Nanoparticle characterization techniques”. In: *Green Synthesis, Characterization and Applications of Nanoparticles*. Elsevier, Jan. 2019, pp. 303–319. DOI: 10.1016/b978-0-08-102579-6.00012-5.

[74] *FT-IR Spectroscopy*. URL: https://www.newport.com/n/introduction-to-ftir-spectroscopy (visited on 06/23/2021).

# A

# Additional figures

## A.1. AFM

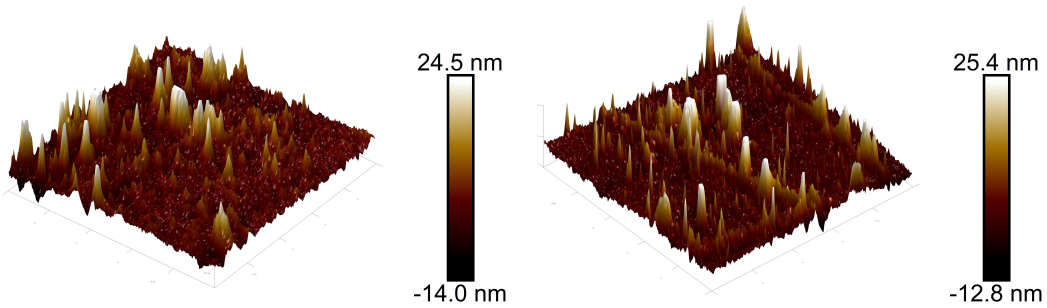


**(a)** 10kGy **(b)** 100kGy

**Figure A.1:** AFM of irradiated PC in wet environment with a dose of 10kGy and 100kGy.

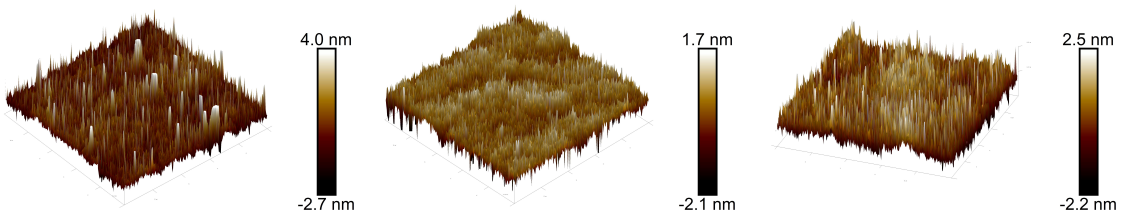


**(a)** 10kGy **(b)** 100kGy **(c)** 1MGy

**Figure A.2:** AFM of irradiated quartz in wet environment with a dose of 10kGy, 100kGy and, 1MGy

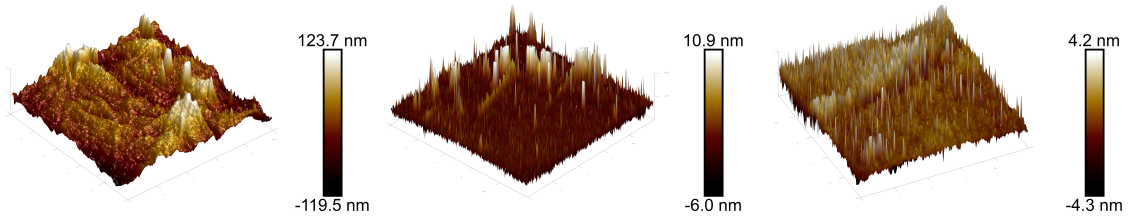


**(a)** AFM of HDPE **(b)** AFM of PC **(c)** AFM of quartz

**Figure A.3:** AFM of electron irradiated HDPE, PC, quartz with a dose of 1MGy

## A.2. SEM images

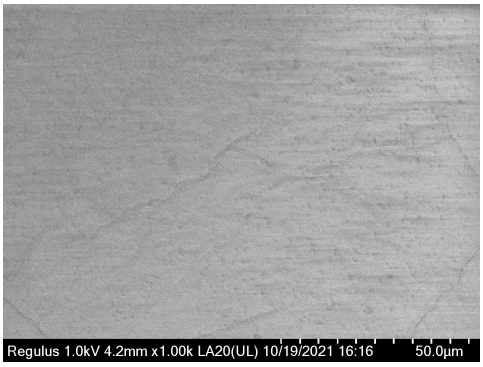


**(a)** SEM of PDMS with APALD at 1k magnification

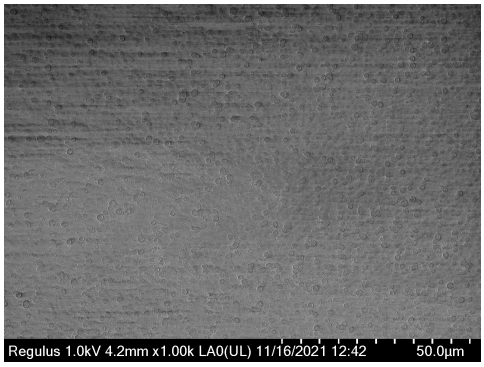


**(b)** SEM of HDPE with APALD at 1k magnification

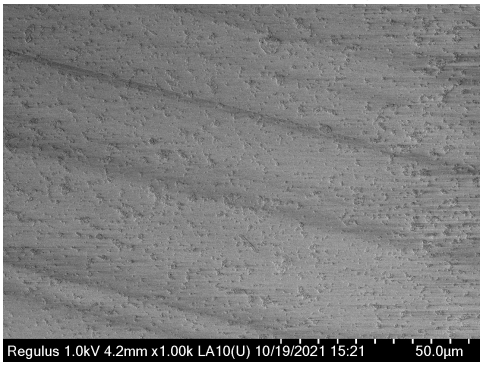


**(c)** SEM of PC with APALD at 1k magnification

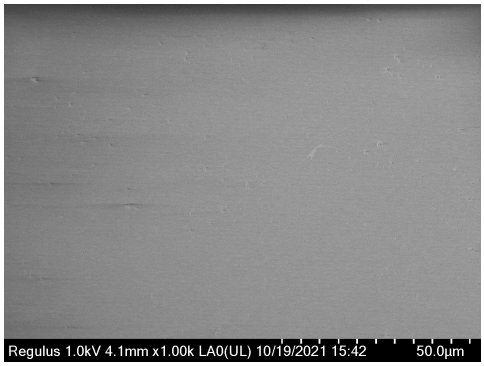


**(d)** SEM of quartz with APALD at 1k magnification

**Figure A.4:** SEM images of PDMS, HDPE, PC and quartz with $TiO_2$ APALD

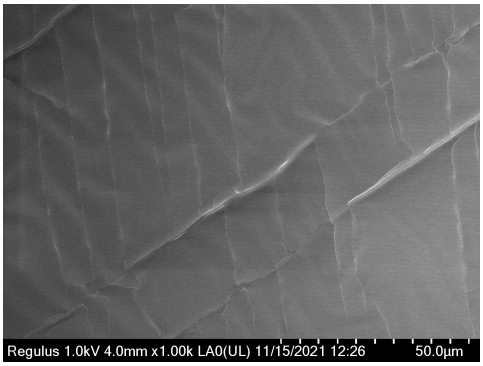


**(a)** SEM of PDMS with VALD at 1k magnification

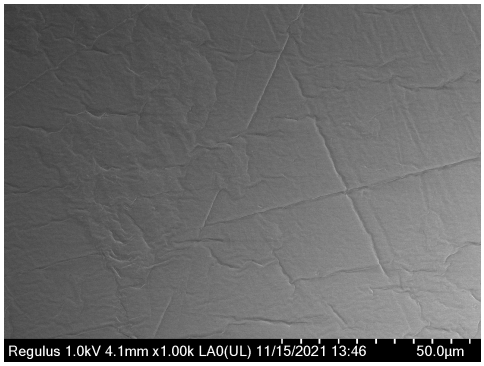


**(b)** SEM of HDPE with VALD at 1k magnification

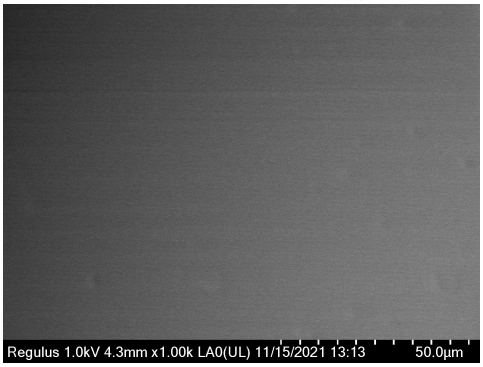


**(c)** SEM of PC with VALD at 1k magnification

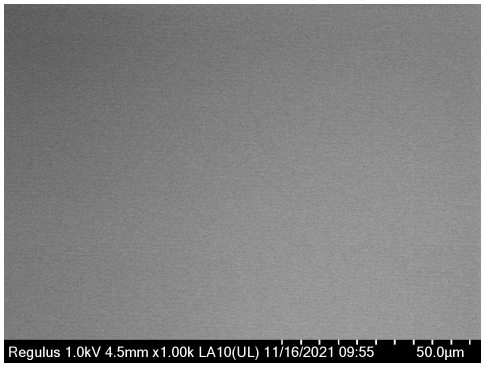


**(d)** SEM of quartz with VALD at 1k magnification

**Figure A.5:** SEM images of PDMS, HDPE, PC and quartz with $TiO_2$ VALD

## A.3. XPS

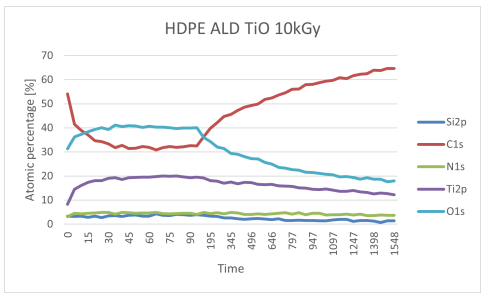


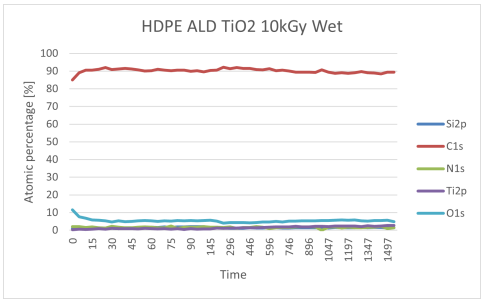


**Figure A.6:** XPS spectra of HDPE in wet and dry environment after 10kGy exposure from a gamma cell

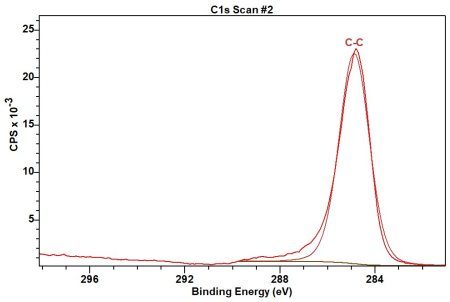


**(a)** HDPE dry

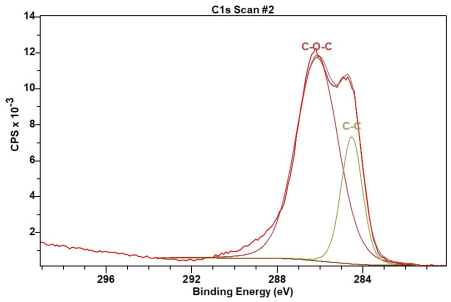


**(b)** HDPE wet

**Figure A.7:** XPS C1s spectra of HDPE in wet and dry environment after 10kGy exposure from a gamma cell

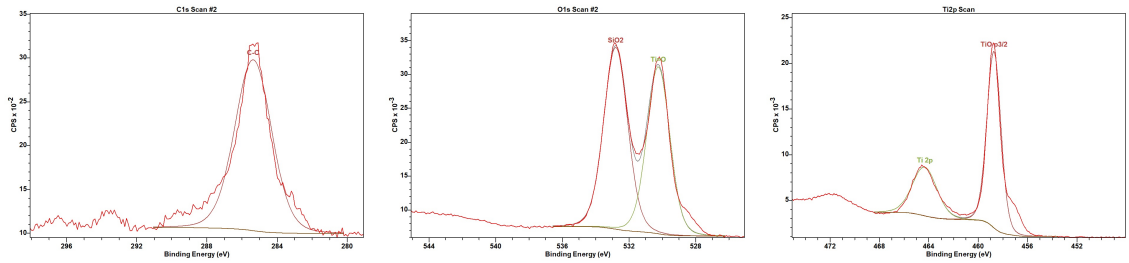


**(a)** C1s spectrum of PDMS VALD **(b)** O1s spectrum of PDMS VALD **(c)** Ti1s spectrum of PDMS VALD

**Figure A.8:** XPS spectrum of PDMS with VALD

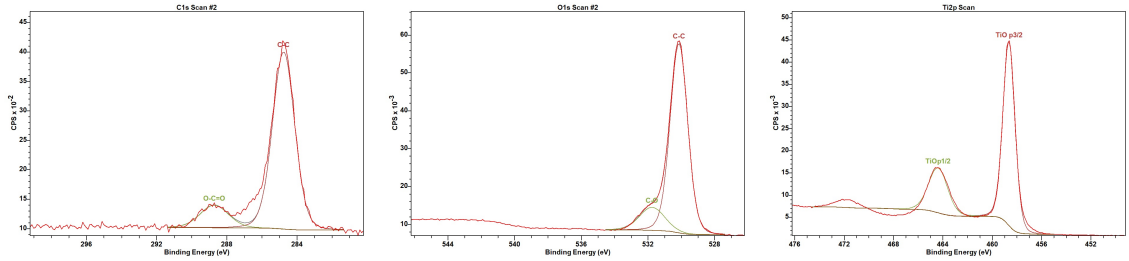


**(a)** C1s spectrum of PC VALD **(b)** O1s spectrum of PC VALD **(c)** Ti1s spectrum of PC VALD

**Figure A.9:** XPS spectrum of PC with VALD

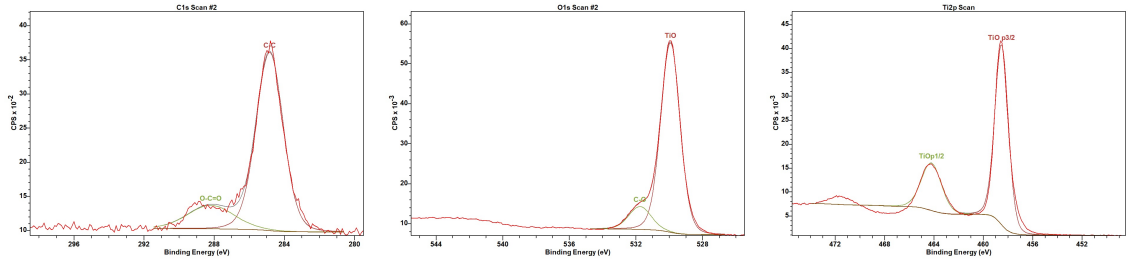


**(a)** C1s spectrum of quartz VALD **(b)** O1s spectrum of quartz VALD **(c)** Ti1s spectrum of quartz VALD

**Figure A.10:** XPS spectrum of quartz with VALD

# A.4. Mechanical compression test

**Figure A.11:** Stress and strain curve of various PDMS samples

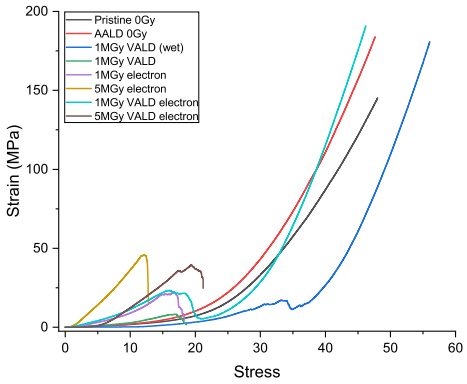


**Figure A.12:** Stress and strain curve of various PDMS/clay samples

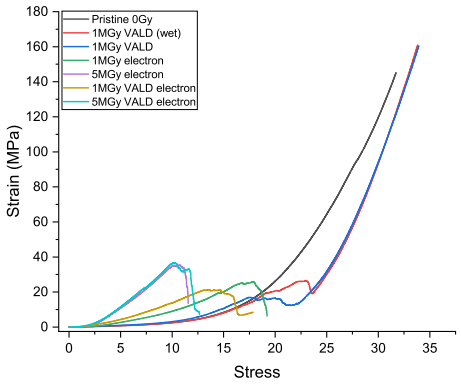


**Figure A.13:** Stress and strain curve of various HDPE samples

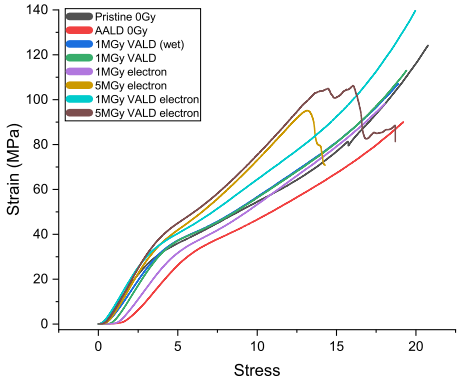


**Figure A.14:** Stress and strain curve of various PC samples

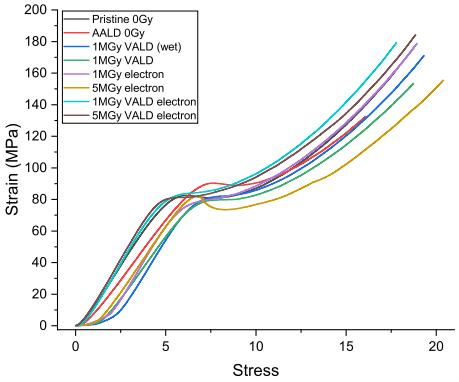


**Figure A.15:** Stress and strain curve of various PS samples

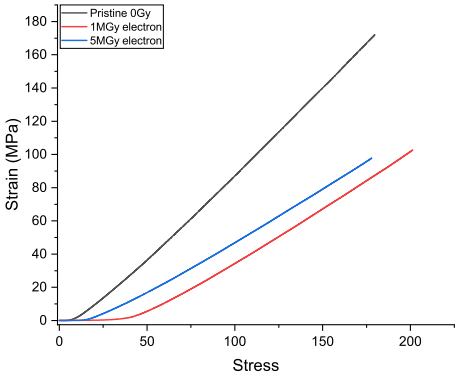


**Figure A.16:** Stress and strain curve of various Quartz samples

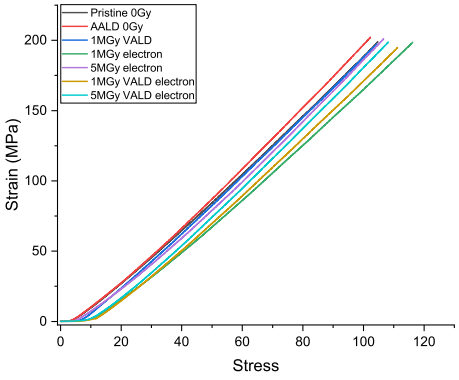

# A.5. XRD

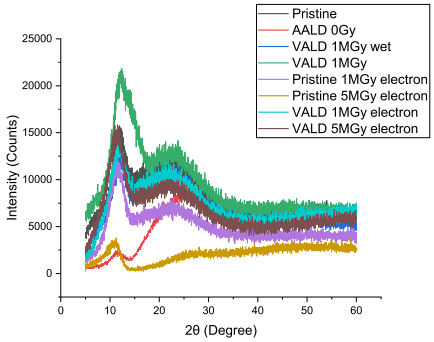


**(a)** XRD of PDMS

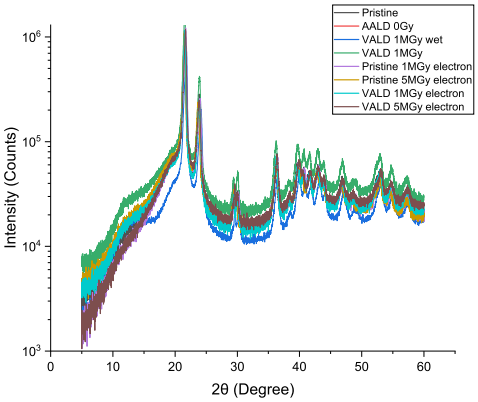


**(b)** XRD of HDPE

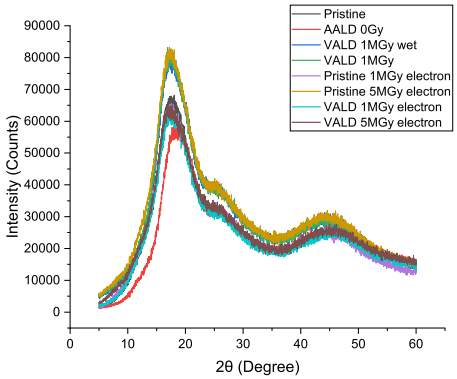


**(c)** XRD of PC

**Figure A.17:** XRD of irradiated and non irradiated materials with(out) coating

# B

# Radiation report

TU Delft

## ELECTRON BEAM IRRADIATION

**test date:** 01-12-2021 **report no:** EB2141

**order date:** 15-11-2021 **purchase order:** -
**ordered by:** Remy Jong, TUD

**executed by:** Lennart van den Hengel, Ferdinand Grozema, Faculty of Applied Sciences, Opto-electronic Materials, Mekelweg 15, 2629JB Delft, E-mail L.vandenhengel@tudelft.nl, Tel. 06-27578269.

**purpose:** 1 MeV irradiation of coated samples.

**accelerator settings:**

| | | | | | | | |
|---|---|---|---|---|---|---|---|
| accel voltage | U | = | 1 | MV | anode | 350 | |
| scan setting | S | = | 300 | mm | focus | 250 | |
| scan width | Sw | = | 200 | mm | bias | 235 | |
| current | $I_e$ | = | 210 | µA | e.m. focus | 0.60 | A |
| table to scanner-distance | H | = | 20 | cm | X-axe | 0 | mm |
| | | | | | Y-axe | -2.0 | mm |

**dosimetry:** Irradiation with a beam current of 208.5 µA beam current resulted in an average dose of 48.0 kGy/cm^2 in 80 seconds.

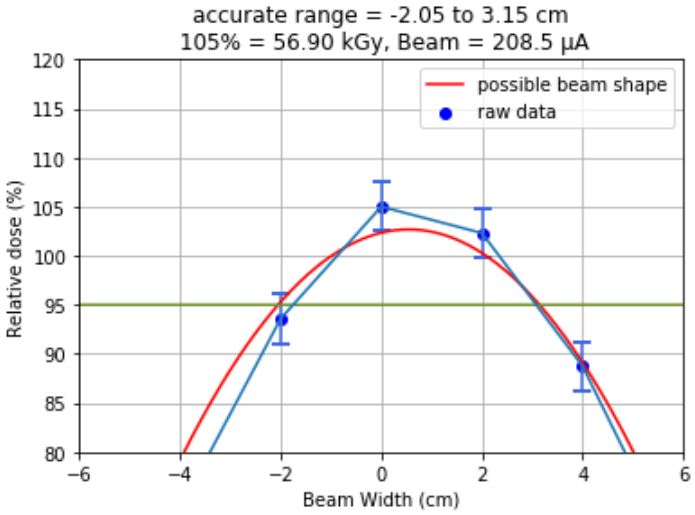


**Figure 1. Dose distribution.**

Beam shape approximated with the function: D = c - a*(x + b)**2 with a = 1.138 b = -0.548 c = 102.68
The standard deviation in parameters a, b and c are respectively 0.0969, 0.1547, 2.0373

The average of 48 kGy in 80 seconds is taken as dose rate at 208.5 µA, a variation in the beam current results in a linear change in the dose rate.

| date | time | sample ID's | I (µA) | D(needed) (Gy/cm^2) | dose rate (kGy/s) | t_needed (s) | time set | exact dose (Gy/cm^2) |
|---|---|---|---|---|---|---|---|---|
| 1-12-2021 | 10:18 | Alle samples | 209.0 | 1.00E+06 | 0.630 | 1588.55 | 1663 | 1.05E+06* |
| 1-12-2021 | 11:16 | some samples removed | 198.7 | 4.00E+06 | 0.647 | 6181.49 | 6182 | 4.00E+06 |

***first run did not take sample size into account so the duration was calculated longer than it should have been. The exact dosis in given in the table. The second irradiation was done properly.**

**conditions:** samples were handled by client only, table temperature was monitored not to have exceeded **40** °C.

**also see:** see irradiation procedure IRI 3.2, M.L. Hom, date 24/07/97

# C

# Characterization methods

In this section„ a brief description of the method is given to understand better how this method will be a helpful characterization method.

## C.1. Scanning electron microscopy

Scanning electron microscopy is often used for basic research, quality control, and failure analysis. Different materials such as metals, alloys, polymers, ceramics, and biological can be examined.

A scanning electron microscope(SEM) consists of four main components: the electron source, column, electron detector, and sample chamber.

Electrons are produced at the electrons source, which is at the top of the column, and accelerated downwards through the column and a combination of apertures and lenses. Combining the apertures and lenses makes it possible to produce a focused beam of electrons thatthat hits the surface. Then, the electron beam can be moved over the sample with scanning coils to collect information.

In SEM, two main types of sample-electron interactions are detected: BSE (Backscattered electrons) and SE(secondary electrons). The BSE are caused by elastic interactions between the beam and the sample. BSE originates from deeper regions in the sample. While inelastic interactions cause SE, they originate from the sample's surface. Therefore, SE and BSE provide different types of information.

BSE results from elastic interactions of the electrons with the sample and is related to the Z number of the atoms. If the Z number is higher, there is a larger atom that is more likely to scatter the electron and therefore produces more BSE signal. This dependence of the amount of signal on the z number makes it possible to differentiate between materials and gives information about the sample's composition. SE originates from the surface of the sample and provides more detailed information on the sample's surface.

When a non-conductive specimen is placed under an SEM, there will be no image output due to the interaction of the negatively charged electron with the sample. When the incident electrons reach the sample, they will negatively charge it. The result of this process is that the sample will now repel the incoming electrons. So most samples need to be coated with a thin gold or carbon layer to prevent the sample from charging.

## C.2. Atomic force microscopy

With Atomic force microscopy (AFM), it is possible to understand the three-dimensionalthree-dimensional surface better. AFM uses a sharp probe that runs raster scans across the sample's surface with an accuracy in the sub-nanometer range. A nanoscopic probe is moved up and down during the scan to maintain a constant interaction with the sample. These up and down movements are recorded against the XY position to create a surface topography of the sample. Then, the probe is positioned with a piezoelectric scanner where the movements are driven by high voltages.

A microcantilever with a sharp tip is attached to the probe. The tips diameter ranges from a few nm to 30nm. The microcantilever can be around 125-450$\mu$m in length and 30-40$\mu$m in width. The

cantilever is the sensor to detect the probe-sample interaction. However, the interaction between the probe and the surface is complicated as many types of forces are involved. In this section, only a few aspects related to the AFM and the applications are discussed.

The bending of the cantilever during the interaction of the probe and sample can be expressed in the normal force according to Hooks' law (see Equation C.1). Where k is the spring constant of the cantilever, and $\Delta$z is the bending of the cantilever in nm.

$$F = k\Delta z \tag{C.1}$$

These cantilevers can measure forces between en few pN up to a few hundreds of $\mu$N. The cantilever is also tracked precisely by a laser beam to measure the slight bending or twisting of the cantilever. The laser beam is focused on the end of the cantilever and reflected towards a quadrant photo-diode as seen in Figure C.1. This diode is also known as a position-sensitive photo-diode (PSDP). When the cantilever bends, the direction of the reflected laser changes accordingly. The position of the laser beam is indicated by the output of PSPD. However, the PSDP measures the angle of deflection and not the displacement.

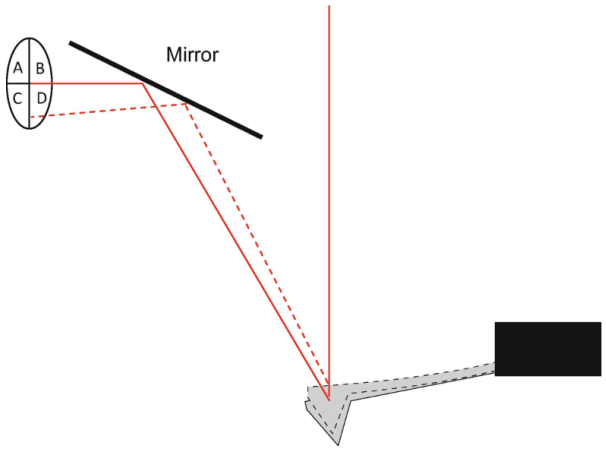


**Figure C.1:** Cantilever with a quadrant photo-diode.

**Contact mode**

Suppose the AFM is used in contact mode. The normal force in maintained constant during the scan. So when the probe comes across a protrusion, the cantilever is pushed up and creates a vertical deflection. This deflection needs to be corrected, and the probe will be lifted up until the deflection becomes zero and vice versa. In combination with a feedback loop, the probe tracks the surface to create a topological overview of the sample. During the scan, there is also a frictional force present which provides information about the local friction, but it also causes some problems. For example, if the probe is not controlled correctly, it can cause damage to delicate samples and the sharp tip. To minimize these consequences, a sub nN force control is needed. Therefore plays the cantilever spring constant a critical role. When the cantilever is softer, it deflects more under the same load, which is positive for the sensitivity of the force detection. However, some disadvantages will occur with the use of a softer cantilever. They will suffer more from thermal drift with the temperature variation caused by the laser beam. This drift causes errors in the imaging process.

**Tapping mode**

If the AFM is used in the tapping mode, the cantilever oscillates at its resonance frequency. This can be done by a small piezoelectric material that is embedded in the probe. To measure the cantilever oscillation, the output of the PSPD is used. With an engaging mechanism, the probe is brought to the sample surface, where interaction occurs between the sample and probe. At the lowest point of the amplitude of the cantilever, the sharp tip contacts the surface. When a protrusion is present on the surface, it will decrease the amplitude of the cantilever and vice versa. During the XY raster scan, the probe is moved up and down to maintain constant amplitude. These up and down movements of

the probe are used to create a topographical overview of the surface. Next to a change in amplitude also, a time lag is recorded. This is measured by the phase difference between the cantilever and the drive signal. This time lag is caused by the energy dissipation during an oscillation cycle. If the probe touches the sample, it undergoes deformations which cause energy to lose. When the tip retracts from the surface, it needs to overcome the adhesive force. This interaction gives information about the viscoelastic properties of the sample and can be used to differentiate between different materials.

## C.3. X-ray photoelectron spectroscopy

X-ray photoelectron spectroscopy (XPS) is a method to analyze the chemical composition of surfaces. XPS is based upon the photoelectric effect, which is discussed in Section 2.1.1. An X-ray light ionizes the molecules, and the electrons from at least the highest valence shell get ejected. When high energy is used, the electrons from deeper levels may be ejected. To characterize the chemical composition, the kinetic energy of the ejected electron is studied in spectroscopy. This can be done by sending in photons with known energy. When the electron is ejected, there is a loss of binding energy, which is equivalent to the binding energy. The kinetic energy can be described as:

$$Kineticenergy = hv - Be - \oslash S \tag{C.2}$$

Where hv is the energy of the photon, Be is the binding energy of the electron in the specific orbital, and $\oslash S$ is the work function of the spectrometer. An XPS spectrum overview is illustrated in Figure C.2

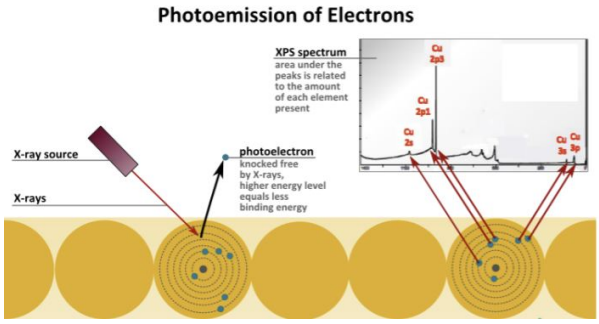


**Figure C.2:** Overview of a photoemission of electrons[72]

With the XPS spectrum, it is possible to see how many electrons are detected with respect to their kinetic energy. This spectrum gives more insight into the electron energy distribution of the specific material. Each element has its own characteristic peaks due to the characteristic binding energy of each element. With this, each material can be analyzed because each peak correspond to the different electron configuration in different orbitals(i.e., 1s,2s,2p, etc.).

## C.4. Fourier-transform infrared spectroscopy

Fourier transform infrared spectroscopy (FTIR) is used for the identification of inorganic, organic, and polymeric materials. FTIR is helpful in identifying unknown materials; it can detect contaminants in materials, find additives and identify decomposition and oxidation. This all can be done by measuring alterations in the characteristic pattern of the absorption bands.

As seen in Figure C.3, the setup consists of a beam splitter, a fixed mirror, and a mirror that can translate back and forth. Infrared radiation emission is sent out by the source towards the beam splitter. The purpose of the beam splitter is to transmit half of the radiation and to reflect the other half. The transmitted beam reaches the fixed mirror, while the reflected beam reaches the moving mirror. After both beams are reflected back, due to the mirrors, they reach the beam splitter again. Where half of the radiation is transmitted, and half of the radiation is reflected. In the end, one beam is passing to the detector while the other beam is sent back to the source. This gives us the optical path difference (OPD), which is the difference between the two beams that traveled through the interferometer. The OPD can be calculated with OPD = $2\Delta$n. The OPD is the product of the distance traveled by the moving mirror multiplied by 2, 4, or another multiplier which is a function of the number of mirrors used. This

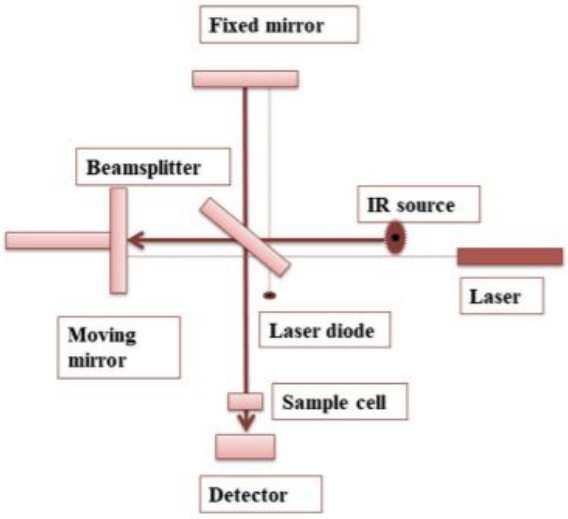


**Figure C.3:** Schematic overview of a interferometer[73]

is also multiplied with n, which is the refraction index of the medium inside the interferometer. This can be just air or nitrogen for purged systems. To determine the distance traveled by the moving mirror, the zero path difference(ZPD) can be used. This is a reference point when the fixed and moving mirrors have the same distance to the beam splitter.

The result of an FTIR is given in an interferogram. An example is given in Figure C.4.

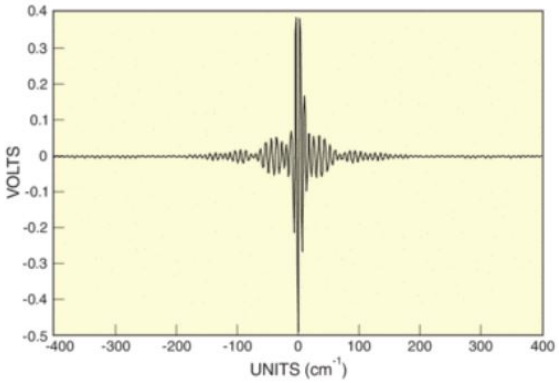


**Figure C.4:** Broadband source interferogram [74]

The big amplitude in the middle is the signature of a broadband interferogram. This is a result of all the wavelengths that are in phase with the ZPD, which means that their contribution towards the signal is at its maximum. When there is an increase in the OPD, the different wavelengths produce peaks at different positions. Because it is a broadband signal, the peaks will never reach their maximum at the same time. This is the reason why the Interferogram is a decreasing oscillating signal.